Master Thesis

"Climate Physics: Physical Oceanography and Meteorology"

Christian-Albrechts-Universität zu Kiel

Mathematisch-Naturwissenschaftliche Fakultät

Intraseasonal Variability of the Equatorial Atlantic Ocean

Franz Philip Tuchen
Matrikel-Nummer: 5682
Kiel, 28.11.2016

First Supervisor: Prof. Dr. Peter Brandt
Second Supervisor: Dr. Martin Claus

GEOMAR
Helmholtz Centre for Ocean Research Kiel

C A U
Christian-Albrechts-Universität zu Kiel

Abstract

Intraseasonal meridional velocity variability and its impact on the deep equatorial circulation is analysed by using a newly assembled data set of equatorial horizontal velocities at 23°W covering the period December 2001 - September 2015.
While zonal velocity variability is mainly focused on three distinct signals (semi-annual, annual, interannual) meridional velocity variability is dominated by intraseasonal fluctuations (15-40 days) due to Tropical Instability Waves (TIWs) at the surface which furthermore excite downward- and eastward-propagating Yanai Waves (or mixed Rossby-Gravity Wave) beams with similar frequencies. The strength of TIWs undergoes a semi-annual cycle with a strong maximum in boreal summer-autumn (July-October) and a weaker maximum in winter (December-January). The upward phase propagation of single Yanai Wave beams is relatively constant within the same beam but differs between different beams. A vertical mode decomposition shows that Deep Equatorial Intraseasonal Variability (DEIV) can be mainly associated with Yanai Wave propagation from the near-surface into the deep ocean; at least for the second baroclinic and higher modes. The first baroclinic and the barotropic mode contain variability in the intraseasonal frequency range as well but a separation between Yanai Wave and Rossby Wave dynamics is not possible without information of the zonal wavenumber. The three distinct zonal velocity signals are located on the resonant basin mode frequency line suggesting the linearity of the Equatorial Deep Jets (EDJs).
Eventually the calculation of a time series for meridional Reynolds-Stress gradients based on two additional moorings north and south of the equator indicates a positive correlation between the interannual variability of the Reynolds-Stress gradient and interannual zonal velocity variability at the equator in a certain depth giving evidence that intraseasonal variability - mainly due to Yanai Waves - is capable of maintaining the interannual Equatorial Deep Jets (EDJs). To our knowledge this is the first observational work that indicates this connection.

Zusammenfassung

Intrasaisonale meridionale Geschwindigkeits-Variabilität und deren Einfluss auf die tiefe äquatoriale Zirkulation werden auf der Grundlage eines neu zusammengesetzten Datensatzes von äquatorialen Horizontalgeschwindigkeiten bei 23°W und für eine Periode von Dezember 2001 - September 2015 analysiert.
Während sich die zonale Geschwindigkeits-Variabilität auf drei diskrete Signale (semi-annuale, annuale, zwischenjährliche Schwankungen) konzentriert, ist bei der meridionalen Geschwindigkeits-Variabilität festgestellt worden, dass diese von intrasaisonalen Fluktuationen (15-40 Tage) dominiert wird. Diese Schwankungen werden an der Meeresoberfläche von tropischen Instabilitätswellen (TIWs) angeregt, welche darüber hinaus Yanai-Wellen (planetare Schwere-Wellen) erzeugen, die mit einer ähnlichen Frequenz herunter und ostwärts propagieren. Die Stärke der TIWs unterliegt einem halbjährlichen Gang mit einem starken Maximum im borealen Sommer-Herbst (Juli-Oktober) und einem schwächeren Maximum im borealen Winter (Dezember-Januar). Die nach oben gerichtete Phasengeschwindigkeit der einzelnen Yanai-Wellen ist relativ konstant innerhalb eines Strahls, variiert jedoch zwischen verschiedenen Strahlen. Eine vertikale Modenzerlegung zeigt weiter, dass die tiefe äquatoriale intrasaisonale Variabilität (DEIV) hauptsächlich mit der Propagation von Yanai-Wellen in Verbindung gebracht werden kann. Diese Aussage trifft für den zweiten baroklinen Mode und höhere Moden zu. Der erste barokline und der barotrope Mode zeigen ebenfalls hohe Amplituden im intrasaisonalen Bereich, können jedoch nicht klar den Yanai-Wellen oder den Rossby-Wellen zugeordnet werden, da dies Informationen über die zonale Wellenzahl benötigen würde. Die drei diskreten Signale der zonalen Geschwindigkeits-Variabilität liegen auf der Linie der resonanten Beckenmodenfrequenz, was auf die Linearität der äquatorialen Tiefen-Jets (EDJs) hindeutet.
Abschließend zeigt die Berechnung einer Zeitserie des meridionalen Reynolds-Stress-Gradienten durch zwei weitere Verankerungen nördlich und südlich des Äquators, dass eine positive Korrelation zwischen der zwischenjährlichen Variabilität dieses Gradienten und der zwischenjährlichen, äquatorialen Zonal-Geschwindigkeits-Variabilität in einer bestimmten Tiefe vorliegt. Dies deutet daraufhin, dass intrasaisonale Variabilität, hauptsächlich erzeugt durch Yanai-Wellen, erklären könnte, wie die EDJs aufrechterhalten werden. Unseres Wissens nach ist dies die erste Arbeit, die diesen Zusammenhang auf der Grundlage von Beobachtungsdaten beschreibt.

Contents

1 Introduction

The Equatorial Atlantic Ocean is characterized by a complex set of strong zonal currents. Figure 1.1 shows the tropical mean zonal velocity from meridional ship sections between 1999-2008 in the top 1000m. The strongest current is the eastward flowing Equatorial Undercurrent (EUC; see Table 1.1 for a full list of all abbreviations used in this work) in the thermocline layer with mean zonal velocities of more than 60 $\frac{cm}{s}$ (e.g. *Brandt et al.* [2014]). Below the EUC vertically alternating zonal jets, the so called Equatorial Deep Jets (EDJs), are observed but do not appear in the mean section because the time span of measurements is about two times longer than the period of the EDJs which is approximately 4.5 years (e.g. *Brandt et al.* [2011]). The observed mean westward flow underneath the EUC belongs to the Equatorial Intermediate Current (EIC). The EDJs were first described in the Indian Ocean by *Luyten and Swallow* [1976] and later in the Atlantic Ocean by *Eriksen* [1982]. On interannual time scales the EDJs are the dominant mode of zonal velocity variability at intermediate depths in the Atlantic Ocean (*Brandt et al.* [2011], *Claus et al.* [2016]) but although their characteristics have been described continuously in the past 15 years on the basis of observational data (e.g. *Johnson and Zhang* [2003], *Bunge et al.* [2008], *Brandt et al.* [2008], *Brandt et al.* [2011], *Brandt et al.* [2012]) their forcing mechanism is still not fully understood and it is an essential part of the ongoing research which - so far - is mainly based on numerical simulations (e.g. *D'Orgeville et al.* [2007], *Hua et al.* [2008], *Ascani et al.* [2010], *Ascani et al.* [2015]).
There are different proposed mechanisms which will be explained more in detail in section 1.4.3. *D'Orgeville et al.* [2007] showed that in their primitive equation model an oscillatory western boundary current excites mixed Rossby-Gravity Waves (or Yanai Waves) propagating eastward along the equator at depth (see also *Eden and Dengler* [2008]). These intraseasonal wave trains are subsequently destabilized, forcing equatorial jets with higher vertical mode. Yanai Waves are strongly destabilized by e.g. barotropic instabilities from the meridional shear of the wave (*Hua et al.* [2008]). Another proposed mechanism was recently presented by *Ascani et al.* [2015] who numerically showed that short intraseasonal Yanai Waves interact non-linearly via the meridional advection term ($v\frac{\partial u}{\partial y}$) from the zonal momentum equation and excite vertically alternating zonal jets comparable to observational EDJs. However *Ascani et al.* [2015] were able to explain the maintenance of the jets but not the observed vertical scale and propagation. To date all proposed forcing mechanisms are based on idealized numerical simulations.
Previous studies have shown the importance of Yanai Waves and intraseasonal meridional variability in general as part of the forcing mechanism of EDJs. A more detailed description of their characteristics is needed for a better understanding of the complex process of forcing and maintaining the Atlantic EDJs. Within the framework of this Master Thesis

a large data set of moored equatorial velocities is analysed. The present work focuses on the description of meridional intraseasonal variability and tries to quantify their influence on the excitation and maintenance of zonal interannual velocity variability in the form of EDJs. Therefore it is - to our knowledge - the first scientific work that describes intraseasonal variability in the Equatorial Atlantic Ocean with such a long observational data set and also in previously undescribed depths.

Abbreviation	**Meaning**
AMOC	Atlantic Meridional Overturning Circulation
cSEC	central South Equatorial Current
DEC	Deep Equatorial Circulation
DEIV	Deep Equatorial Intraseasonal Variability
EDJ	Equatorial Deep Jets
EIC	Equatorial Intermediate Current
EICS	Equatorial Intermediate Current System
EUC	Equatorial Undercurrent
ITCZ	Intertropical Convergence Zone
NBC	North Brazil Current
NEC	North Equatorial Current
NECC	North Equatorial Counter Current
nNECC	northern North Equatorial Counter Current
NEUC	North Equatorial Undercurrent
NICC	Northern Intermediate Counter Current
nSEC	northern South Equatorial Current
OGCM	Ocean General Circulation Model
POP	Principal Oscillation Pattern
SEC	South Equatorial Current
SEUC	South Equatorial Undercurrent
SICC	Southern Intermediate Counter Current
SST	Sea Surface Temperature
TC	Tropical Cells
TIW	Tropical Instability Wave

Table 1.1: *List of all abbreviations used in this work in alphabetical order.*

This work is organised as follows: In the first chapter the physical background of the Equatorial Atlantic Ocean will be described including the mean state of the circulation, Tropical Instability Waves (TIWs), variability in the zonal and meridional velocity component, their forcings and impacts. Chapter two gives an overview of the data used for the analysis done here and explains the mathematical methods. In the third chapter the results are shown and divided into spectral analysis, Tropical Instability Waves, characteristics of certain Yanai beams, vertical mode analysis and Reynolds-Stress. Lastly the fourth chapter summarises the results from chapter three for a critical discussion of the

importance and relevance of the presented findings and compares them to theoretical and observational studies.

1.1 The Equatorial Atlantic Ocean mean circulation

The current system of equatorial oceans is generally a set of zonal currents within the basin but framed at the boundaries by currents which are under the influence of the coastline. Here we want to focus on the mean state of the equatorial circulation in the Atlantic Ocean. As shown in Figure 1.1 a meridional mean section of the Tropical Atlantic reveals a variety of zonal currents, of which the eastward Equatorial Undercurrent (EUC) between 2°N and 2°S is the strongest with mean zonal velocities of more than 60 $\frac{cm}{s}$ (*Cromwell et al.* [1954], *Brandt et al.* [2014]) but reaching up to 100 $\frac{cm}{s}$ in peak while having its mean core depth at about 80m (*Brandt et al.* [2011]). The EUC follows an eastward pressure gradient that is generated by westward blowing trade winds (Easterlies) in the Equatorial Atlantic and transports oxygen-rich and high-saline water masses from the western boundary eastward into the ocean basin at the thermocline layer (*Metcalf et al.* [1962]) contributing both to the Atlantic Meridional Overturning Circulation (AMOC) and the wind-driven subtropical cells (*Hazeleger et al.* [2003]). Its main role is the supply of thermocline waters from the shallow subduction zones in the subtropics to the main upwelling zones in the central and eastern part of the Atlantic Ocean (*Schott et al.* [1998]). *Brandt et al.* [2014] showed that the strong seasonality of the EUC is dominated by an annual harmonic of the EUC transport and the EUC core depth with maxima during late boreal summer and a semi-annual harmonic of the EUC core velocity with maxima in boreal spring and late boreal summer. On interannual time scales the EUC transport shows variability in accordance with anomalous Equatorial Atlantic cold tongue events while the meridional position of the EUC varies on timescales close to the 4.5 year EDJ-cycle (*Brandt et al.* [2014]). At the surface and close to the equator westward surface currents are generated due to the continuous wind stress forcing of the Easterlies (*Lumpkin and Garzoli* [2005]). At 2°N the northern branch of the South Equatorial

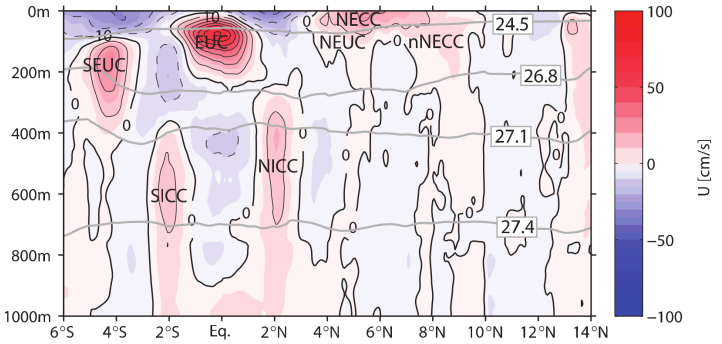

Figure 1.1: *Mean zonal velocity from meridional ship sections between 28.5°-23°W during 1999-2008. Red indicates eastward flow, blue indicates westward flow. Isopycnals are shown in grey solid lines. For abbreviations see Table 1.1. Taken from Brandt et al. [2010].*

Current (nSEC) and at 4°S the central branch (cSEC; sometimes called equatorial South Equatorial Current (eSEC), e.g. in *Schott et al.* [1998] and *Brandt et al.* [2008]) frame the EUC and build shear regions at the transition zones due to their contrary flow directions. Especially the horizontal shear region between the EUC and the nSEC is a source of barotropic instabilities which subsequently maintain and modulate Tropical Instability Waves (TIWs) (*Qiao and Weisberg* [1998]).

Figure 1.2 shows a schematic of the Tropical Atlantic surface circulation which is bounded by the northern and southern hemisphere subtropical gyres and forms a clockwise equatorial gyre. At the eastern boundary the South Equatorial Current (SEC) is excited and separated at around 5°W into a northern and central branch. The central branch of the SEC bifurcates at the western boundary into the North Brazil Current (NBC) to the north and into the Brazil Current to the south. The NBC is the western boundary current of the equatorial gyre. It flows northward, crosses the equator and partly retroflects eastward into the EUC (e.g. *Lumpkin and Garzoli* [2005]) while the remaining NBC flows further north until it retroflects at 7°N into the eastward flowing North Equatorial Counter Current (NECC). At the retroflection point eddies are generated which propagate north-westward along the coast and contribute to the interhemispheric exchange of mass and heat associated with the upper limb of the AMOC (*Garzoli et al.* [2003]).

At around 5°-7°N the North Equatorial Counter Current (NECC) flows eastward and hits the African coast, from where it is called the Guinea Current which flows along the coast and eventually closes the equatorial gyre. The NECC is strongest during boreal summer (*Peterson and Stramma* [1991]) driven by the large-scale seasonality of the trade winds and the seasonal shift of the Intertropical Convergence Zone (ITCZ) (*Stramma and Schott* [1999]). The southernmost location of the ITCZ in boreal spring leads to a weakening or even reversed westward flow of the NECC (*Schott et al.* [1998]). Between the NECC and the northern branch of the SEC another strong horizontal shear region is found. Together with the shear between the nSEC and EUC (*Jochum and Murtugudde* [2004]) these two regions are believed to be responsible for the generation of Tropical Instability Waves (TIWs) due to the meridional shear of the zonal currents which produces barotropic instabilities (*von Schuckmann et al.* [2008]). In the southern hemisphere TIWs are forced exclusively by baroclinic instabilities while for the northern hemisphere *von Schuckmann et al.* [2008] showed that both barotropic instabilities due to the horizontal shears between nSEC/NECC and nSEC/EUC and baroclinic instability due to the vertical shear of the nSEC contribute to the generation of TIWs. Calculations of seasonal changes of the instability production rate of the nSEC/NECC shear showed relatively high values suggesting that the strong seasonality of the NECC dominates the seasonal cycle of the TIWs at this latitude.

At intermediate depth Figure 1.1 reveals a meridional alternation of zonal currents. Below the EUC the westward flowing Equatorial Intermediate Current (EIC) is observed with

two surrounding eastward flowing cores at around 2° off the equator: the Northern and Southern Intermediate Counter Current (NICC and SICC) with mean zonal velocities of 10-15 $\frac{cm}{s}$ (e.g. *Schott* [2003], *Brandt et al.* [2006]) which are also called extra-equatorial jets (*Gouriou et al.* [2001], *Ménesguen et al.* [2009]). The Equatorial Intermediate Current System (EICS) is believed to be similarly generated as the EDJs. As for the EDJs *D'Orgeville et al.* [2007] and *Hua et al.* [2008] suggested instabilites of intraseasonal Yanai Waves as a generation mechanism.

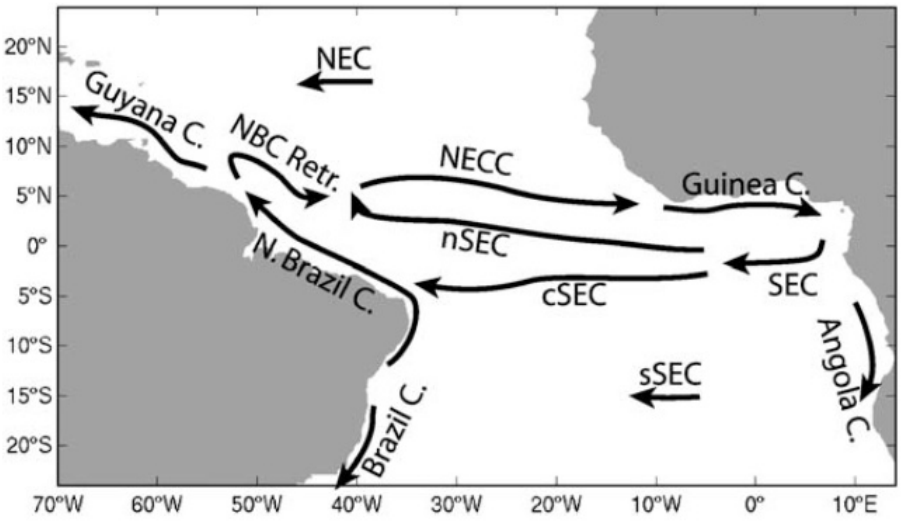

Figure 1.2: *Schematic of the mean surface currents in the Tropical Atlantic Ocean based on drifter observations. The abbreviations are explained in the text. Taken from Lumpkin and Garzoli [2005].*

The mean cross-equatorial structure of meridional velocities is dominated by shallow near-surface overturning cells in the upper 100m, the so called tropical cells (TC), located between 5°N and 5°S (e.g. *Perez et al.* [2013]). They are generated by wind-driven equatorial upwelling, poleward wind-driven flow at the surface, off-equatorial downwelling at 3-5° N/S and equatorward geostrophic flow at the subsurface in about 100m depth. The tropical cells are disturbed by the seasonal appearance of the Atlantic cold tongue and associated Tropical Instability Waves close to the surface which are most pronounced in boreal summer due to intensified south-easterly trade winds and increased shear between the equatorial zonal currents.

1.2 Tropical Instability Waves

Tropical Instability Waves (TIWs) are common to both the Equatorial Atlantic and Pacific Ocean (*Chelton et al.* [2000]). They are often described as undulations of the seasonal sea-surface temperature (SST) between 5°N-5°S but are visible in sea surface height anomalies and meridional velocities as well. Figure 1.3 shows the characteristic SST structure of TIWs for two different time periods in 1998 from satellite measurements. The TIWs appear as near-surface waves with periods of 20-60 days, zonal wavelengths of 400-1500km, westward phase speeds of 20-60 $\frac{cm}{s}$ and a stronger signature in the northern hemisphere (e.g. *Steger and Carton* [1991], *Qiao and Weisberg* [1995]).
Athie and Marin [2008] noted that there are two different sources of Tropical Instability Waves. The first one results from barotropic instabilities (e.g. *Philander* [1978]) arising from the horizontal velocity shear of seasonally varying zonal currents: at the surface between the nSEC and NECC or within the thermocline layer between the nSEC and EUC (see Figure 1.1). Barotropic instabilities obtain their energy from the mean background flow (kinetic energy). The second source is baroclinic instability, e.g. due to the equatorial upwelling front, the vertical shear of the northern South Equatorial Current (nSEC) (*von Schuckmann et al.* [2008]) or the meridionally shoaling thermocline (e.g. *Yu et al.* [1995]). Baroclinic instability requires the presence of horizontal density gradients causing horizontal variability of geostrophic flow with depth. In contrast to barotropic instabilities, baroclinic instabilities obtain their energy from the stratified water column (potential energy). It is believed that both types of instability contribute to the generation of TIWs in the Atlantic Ocean (*Jochum et al.* [2004], *Grodsky et al.* [2005]).

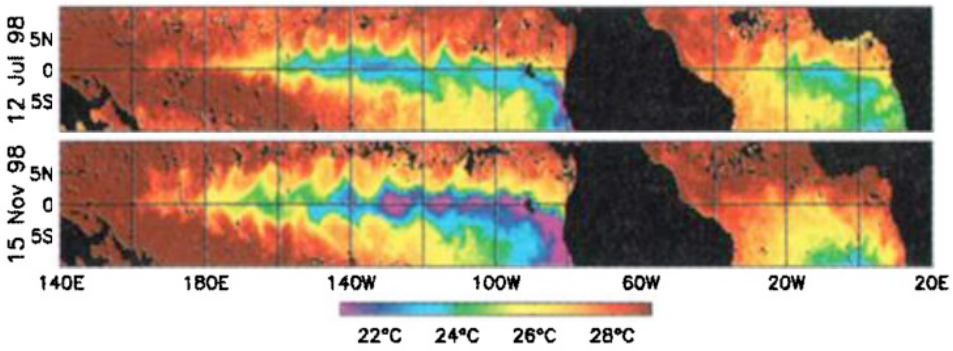

Figure 1.3: *3-day composite-average maps of SST from satellite measurements for 11-13 July 1998 (top) and 14-16 November 1998 (bottom). Black represents land or rain contamination. Taken from Chelton et al. [2000].*

The propagation of Tropical Instability Waves can be explained either as westward propagating Rossby Waves along 5°N with periods greater than 30 days (*Jochum and Malanotte-Rizzoli* [2003]) or as mixed Rossby-Gravity Waves (hereafter called Yanai Waves) close to

the equator with periods within the intraseasonal time scale between 15-40 days (*Düing et al.* [1975], *Weisberg et al.* [1979]). As mentioned above TIWs have a larger amplitude in the northern hemisphere but also occur in the southern hemisphere (*Steger and Carton* [1991]). *Bunge et al.* [2007] suggested different forcing mechanisms for northern and southern hemispheric TIWs since they could not find clear relations between the two signatures in SST. The interannual variability of TIW activity is significant (*Steger and Carton* [1991]) and often related to changes of the intensity of the Equatorial Atlantic cold tongue. More precisely, the period and position of TIWs depend on the timing of the seasonal equatorial cold tongue while larger wavelengths and faster phase speeds are associated with stronger equatorial upwelling (*Athie and Marin* [2008])

TIWs have a significant impact on the mixed layer heat budget due to two processes: advective and diapycnal heat fluxes. During summer, when the equatorial cold tongue is most pronounced, horizontal temperature gradients develop. Tropical Instability Waves disturb this sea-surface temperature front by advecting warm water into regions of cold water and vice versa. When the water parcels return to their initial position a net heat flux has occured. This heat flux is mainly executed meridionally (1°-2°C per month) and less zonally (0.5°-1°C per month) into the cold tongue (*Jochum et al.* [2007]). Additionally microstructure measurements indicate the impact of TIWs on the diapycnal heat flux. During the presence of a TIW elevated turbulence is observed below the mixed layer leading to diapycnal heat flux from the mixed layer into the deep ocean (*Moum et al.* [2009]). *Weisberg and Weingartner* [1988] estimated the equatorward heat flux of the TIWs in the upper 50m with 100 $\frac{W}{m^2}$ which is comparable to the atmospheric heat flux.

Since TIWs disturb SST fronts they furthermore have an impact on the momentum flux by projecting their mesoscale cusp-like structure onto the surface wind stress. Winds tend to be stronger over warm water and weaker over cold water (*Chelton et al.* [2001]) which effects the stratification of the atmospheric boundary laver. A flow from warm to cold SST increases the stratification and consequently decreases near-surface wind stress while the effect reverses for a flow from cold to warm SST. This way TIWs have a strong impact on local atmospheric pressure gradients and changes of the wind stress curl which further influences local weather.

Eventually Tropical Instability Waves are the main source for Yanai Waves at the equator. Parts of the energy of TIWs is radiated into the deep ocean as intraseasonal Yanai Wave beams which will be discussed in 1.3.1.

1.3 Meridional velocity variability

Observations of equatorial zonal and meridional velocity variability reveal two very different spectra for the two horizontal velocity components (*Bunge et al.* [2008]). The zonal velocity spectrum is dominated by variability with longer periods in contrast to the

meridional velocity spectrum which shows peaks in the intraseasonal (10-50 days period) frequency range. *Philander* [1978] noted that this is due to the presence of equatorial waves. Variability on long time scales is associated with equatorial Kelvin and Rossby Waves. Equatorial Kelvin Waves are a completely zonal velocity feature with no associated meridional velocity at all, while equatorial Rossby Waves generate meridional velocities but are limited to lower frequencies. The dispersion diagram for equatorial waves (Figure 1.4) shows that Yanai Waves (called mixed Rossby-Gravity Waves in Figure 1.4) could be an adequate explanation for deep intraseasonal variability in the Tropical Atlantic Ocean. However numerical studies showed that the presence of the mid-Atlantic ridge close to the equator at 23°W could be a source of meridional velocity variability on longer time scales than the distinct intraseasonal signal. *McPhaden and Gill* [1987] numerically showed that a submarine ridge in the path of a propagating equatorial Kelvin Wave generates meridional motions.

1.3.1 Intraseasonal

Observations and numerical simulations show that the dominant signal of meridional velocity variability in the Equatorial Atlantic Ocean is found on intraseasonal (10-50 days period) time scales (e.g. *Ascani et al.* [2015]). Close to the surface the intraseasonal signal is associated with monthly Tropical Instability Waves but in the deep ocean other sources must be responsible. The so called deep equatorial intraseasonal variability (DEIV) is believed to be the source of the deep equatorial circulation (DEC) which includes the EDJs and the Equatorial Intermediate Current System (EICS). In general intraseasonal variability arises from two different sources: Tropical Instability Waves (TIWs) with observed periods between 15-50 days and directly wind-forced intraseasonal variability with periods of approximately 15 days (*Athie and Marin* [2008]).
Realistic numerical simulations showed that a large fraction of the energy that is provided by intraseasonal TIWs radiates into the deep ocean as downward- and eastward-propagating beams of monthly periodic Yanai Waves (*von Schuckmann et al.* [2008], *Ascani et al.* [2010]). Figure 1.4 shows the dispersion relation for equatorial waves in the ω-k (frequency - zonal wavenumber) space. Here the unit of frequency is $\sqrt{\beta c_m}$, where β is the coriolis parameter on an equatorial β-plane with $f = \beta y$ and c_m is the gravity wave speed of the m-th baroclinic vertical mode. The unit of the zonal wavenumber is the inverse of the radius of deformation $\sqrt{\frac{c_m}{\beta}}$. The dispersion relation for Yanai Waves is as follows (*Gill* [1982]):

$$c_Y = \pm c_m \sqrt{\frac{\beta}{k^2 c_m} + \frac{\beta}{\omega k} + 1}$$

Yanai Waves are defined by a single meridional mode. The phase velocity ($\frac{\omega}{k}$) can be either positive or negative which means that Yanai Waves are able to propagate either

eastward or westward while their group velocity ($\frac{\partial\omega}{\partial k}$) is always positive (eastward). They are antisymmetric about the equator in the zonal velocity component but zero at the equator while being symmetric about the equator in the meridional velocity component. Eventually there is only a meridional velocity component at the equator due to Yanai Waves. *Weisberg et al.* [1979] observed a monthly periodic Yanai Wave with upward and westward phase propagation, downward and eastward group propagation and a zonal wavelength of approximately 1200km.

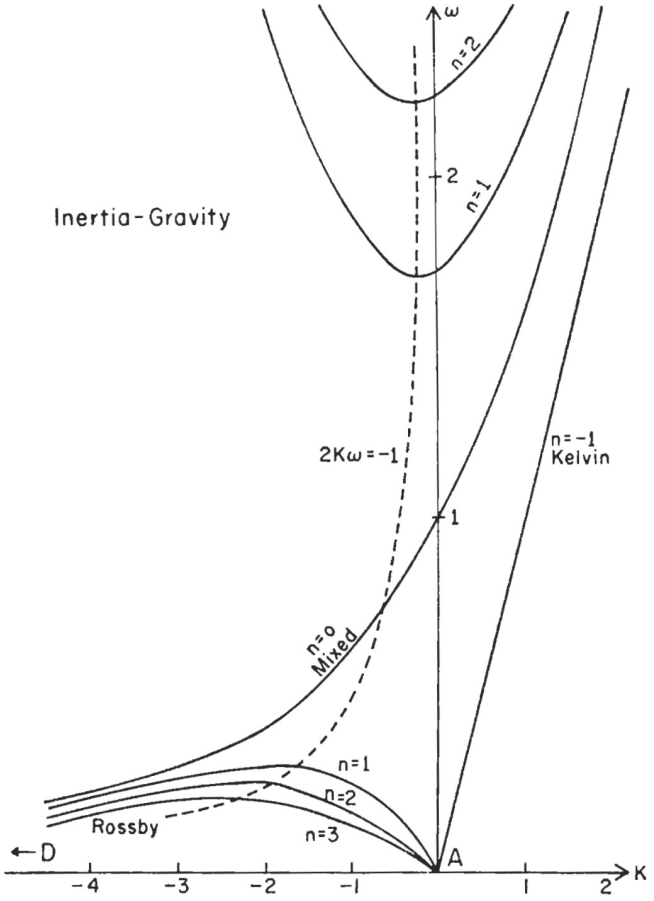

Figure 1.4: *Dispersion relation (ω-k) for waves on an equatorial β-plane for $\omega > 0$. The dashed line connects the extrema and n represents the meridional mode. Taken from Cane and Sarachik [1976].*

Yanai Wave dynamics and interaction are a crucial part of the forcing mechanism of Atlantic EDJs and the Atlantic EICS. *D'Orgeville et al.* [2007] and *Hua et al.* [2008] numerically showed that EDJs and EICS result from the instability of an intraseasonal Yanai Wave, that was generated at the western boundary due to an oscillatory western boundary current. The wave became unstable when reaching a zonal wavelength of about 3° and forced both small-vertical-scale (EDJs) and large-vertical-scale (EICS) motions. *Ascani et al.* [2015] identified two different types of instability. First the self-interaction of Yanai Waves excites EIC-like currents within the wave beam. Secondly Yanai Waves

lose parts of their energy mainly to small-vertical-scale waves (higher baroclinic order). *Ascani et al.* [2015] further showed that high-frequent waves (like Yanai Waves) with high vertical wavenumber arise as part of the interaction, while low vertical wavenumber signals correspond to Tropical Instability Waves (TIWs) which are generated by instabilities of surface equatorial currents. Instability and nonlinear modication of Yanai Waves is consistent with the maintenance of the Deep Equatorial Circulation (DEC). *Ascani et al.* [2010] noted that intraseasonal Yanai Waves are able to modify the potential vorticity of a water parcel when they are breaking due to large amplitudes, further allowing the parcel to have a persistent equatorward drift across potential vorticity contours.

1.4 Zonal velocity variability

Zonal velocity variability can be separated into three dominant periods: semi-annual, annual and interannual. Each of the dominant signals is associated with a vertical baroclinic mode, in which the energy is mostly contained. The second baroclinic mode is associated with the semi-annual cycle, the fourth baroclinic mode is associated with the annual cycle and the 17th baroclinic mode is associated with the interannual Equatorial Deep Jet period of approximately 4.5 years (*Claus et al.* [2016]). It is often noted that the EDJs are similar to the gravest equatorial basin mode (e.g. *D'Orgeville et al.* [2007]) but in fact all three dominant signals are located on the resonance line of the gravest equatorial basin mode which basically consists of an equatorial eastward traveling Kelvin Wave, that is reflected at the eastern boundary into a gravest meridional long Rossby Wave but now propagating at a third of the speed of the Kelvin Wave (*Cane and Moore* [1981]). These three periods can be divided into externally driven (annual and semi-annual) and internally forced (interannual Equatorial Deep Jets). Nevertheless there is also some variability in the zonal velocity component on intraseasonal time scales.

1.4.1 Intraseasonal

Observations show that intraseasonal variability can also be dominated by zonal velocity fluctuations (*Brandt et al.* [2006]) but there is a strong year-to-year variability of these intraseasonal fluctuations which is possibly due to the interannual variability of the equatorial zonal current system. These intraseasonal fluctuations are either westward propagating and associated with TIWs (*Weisberg and Weingartner* [1988]) and vortices (*Foltz et al.* [2004]) or eastward propagating and coming from the western boundary with periods between 35-60 days (*Brandt et al.* [2006]).
Below the near-surface layer fluctuations in the zonal velocity component with shorter periods than the cut-off-period of equatorial Rossby Waves (approximately 32 days for the first meridional and first baroclinic mode) are reducing and meridional velocity vari-

ability dominates (often called the Deep Equatorial Intraseasonal Variability (DEIV) (e.g. *Ascani et al.* [2015])).

1.4.2 Seasonal

The seasonal cycle of equatorial zonal velocity is dominated by an annual cycle and less contributions of a semi-annual cycle. This annual cycle is the dominant zonal velocity variability. (*Brandt et al.* [2006]) showed that an annual harmonic can explain more than 50% of the total variance in some parts of their time series. They also noted that the vertical migration of the EUC core is responsible for maximum eastward flow in April (October) above (below) the mean EUC core. The seasonal upward and downward motion of the EUC is thought to be forced by variations of the wind stress which itself is forced by the seasonal migration of the Intertropical Convergence Zone (e.g. *Provost et al.* [2004], *Johns et al.* [2014]). *Brandt and Eden* [2005] gave evidence that the annual signal below the near-surface layer is dominated by downward propagating lowest odd meridional mode Rossby Waves (dominated by the third and higher baroclinic mode). This causes upward phase propagation which implies downward energy propagation. Their principal oscillation pattern (POP) analysis shows a dominant POP that explains about 70 % of the zonal velocity variability and is clearly connected to the annual cycle. The Rossby Waves are either directly driven by zonal wind anomalies or by wind-driven equatorial Kelvin Waves which have been reflected at the eastern boundary (*Brandt and Eden* [2005]).

1.4.3 Interannual (Equatorial Deep Jets)

On interannual time scales the Equatorial Deep Jets (EDJs) are the dominant signal of variability in the Equatorial Atlantic Ocean. The EDJs are observed in all equatorial oceans. In the 1970s *Luyten and Swallow* [1976] described them first in the Indian Ocean followed by *Hayes and Milburn* [1980] in the Pacific Ocean and lastly by *Eriksen* [1982] in the Atlantic Ocean. In general EDJs are equatorially trapped zonal velocity features which are geostrophically balanced and alternating in direction with depth and time (e.g. *Johnson and Zhang* [2003]). The meridional structure of the EDJs is about 50% wider than expected when considering linear theory based on their observed vertical scale (*Johnson and Zhang* [2003]). *Greatbatch et al.* [2012] showed with their shallow-water model that this discrepancy can be explained by mixing of momentum along isopycnals. Observations of the Atlantic Ocean EDJs, on which we will focus here, show a characteristic vertical scale of 300-700m, an almost basin wide zonal scale, amplitudes of the order of 10-20 $\frac{cm}{s}$ and a period of approximately 4.5 years (*Johnson and Zhang* [2003], *Bunge et al.* [2008]). They are found within a narrow equatorial band of less than 3° latitudinal extent and in depths between the Equatorial Undercurrent at the thermocline (~200m) and approximately 3000m (e.g. *Bourlès* [2003], *Claus et al.* [2014]). The eastward jets supply

the oxygen minimum zone in the deep eastern Atlantic Ocean with dissolved oxygen from the western boundary (e.g. *Brandt et al.* [2008]). In the Atlantic Ocean moored velocity data (e.g. *Bunge et al.* [2008], *Brandt et al.* [2011], *Brandt et al.* [2012], *Claus et al.* [2014], *Claus et al.* [2016]) and hydrographic data analysis (*Johnson and Zhang* [2003]) revealed a downward phase propagation of the deep jets which implies upward energy propagation according to linear theory suggesting an influence of the EDJs on near-surface dynamics and properties.

Brandt et al. [2011] showed that the periodic EDJs have a significant impact on SST, wind and rainfall in the tropical Atlantic region. They give evidence that EDJs are linked to changes of equatorial zonal currents of about 6 $\frac{cm}{s}$ and changes of eastern Atlantic temperature anomalies of about 0.4°C which furthermore can be associated with distinct wind and rainfall patterns. The EDJs propagate energy towards the surface and constitute a 4.5-year cycle of SST, wind and rainfall anomalies in the Tropical Atlantic.

The interannual oscillation of the Atlantic Ocean EDJs is unique compared to the other equatorial ocean basins. In the Pacific Ocean they are known to vary on multidecadal time scales (*Johnson* [2002]) while no dominant signal has been observed in the Indian Ocean. It has to be noted that observational data of EDJs is too short to derive possible multidecadal variabilities for the Atlantic Ocean. EDJs are often associated with the gravest equatorial basin mode (*Cane and Moore* [1981], *D'Orgeville et al.* [2007]) which consists of an equatorial eastward traveling Kelvin Wave which is reflected at the eastern boundary into a gravest meridional mode long Rossby Wave propagating at a third of the speed of the Kelvin Wave.

Vertical mode decomposition showed that the energy associated with the EDJs is distributed between the 10th and the 20th vertical mode with a distinct peak at mode 15 (*Brandt et al.* [2008]) while a more recent study by *Claus et al.* [2016] suggested the vertical baroclinic modes 16 and 17 following the resonance period of the gravest equatorial basin mode close to the 16th and 17th mode.

To date numerical simulations of the EDJs mainly focused on the generation mechanism of the jets but so far models fail to fully reproduce all characteristics of the EDJs. There is a high dependence on the horizontal and vertical resolution of the model which is why eddy-resolving Ocean General Circulation Models (OGCMs) only inconsistently reproduce the jets. For the Atlantic (*Eden and Dengler* [2008]) and Pacific Ocean (*Ishida et al.* [1998]) it was possible to reproduce the jets when a deep cross-equatorial current at the western boundary is included. In both simulations instabilities of a deep western boundary current led to horizonzal energy propagation into the ocean basin due to Kelvin Wave dynamics but both studies failed to reproduce the vertical propagation and low-frequency basin modes. More recent simulations with sufficient horizontal resolution are able to reproduce the EICS but not realistic depths for the extent.

In general there are two proposed forcing mechanisms for the EDJs. First *D'Orgeville*

et al. [2007] and *Hua et al.* [2008] showed that large vertical scale, zonally short Yanai Waves propagate westward and are destabilized by barotropic shear instabilites of the equatorial zonal currents forming zonal jets with small vertical scale. It showed that the zonal scale of the Yanai Waves governs the vertical scale of the jets. Second *Ascani et al.* [2015] recently showed that intraseasonal Yanai Waves - which are generated by barotropic and baroclinic instabilities close to the surface - interact non-linearly via the meridional advection term ($v\frac{\partial u}{\partial y}$) of the zonal momentum equation. The rectification of the DEIV forms small vertical scale jets (EDJs) and large vertical scale currents (EICS) comparable to the observations. Furthermore the EDJs are found to contribute to the maintenance of the EICS which implies a nonlinear energy transfer that is more complex than thought. Nevertheless the approach of *Ascani et al.* [2015] could not explain the vertical scale and the direction of vertical propagation.
However the energy source of the Equatorial Deep Jets is still under debate and is further investigated in this work on the basis of observational moored velocity data.

2 Data and Methods

2.1 Data

Within the framework of this thesis a variety of moored velocity data from 9 mooring periods and almost 14 consecutive years has been assembled (see Figures 2.1 and 2.2). Since 2001 the equatorial 23°W mooring has been maintained and exchanged on a regular basis (except for one period between December 2002 and February 2004, where no mooring was mounted). Table 2.1 shows a list of all equatorial moorings that were used in this work together with the deployment/recovery date and the recovering research cruise. The main purpose of the equatorial 23°W mooring is the detection, measurement and analysis of the equatorial current system both in time and space which is why it is mostly composed of mechanical and acoustical velocity measuring instruments.

Time Period	Mooring	Cruise (Recovery)
14.12.2001 - 21.12.2002	PM-271-A	RV Le Suroit (PIRATA-FR11)
13.02.2004 - 29.05.2005	PM-425-A	RV Le Suroit (PIRATA-FR13)
30.05.2005 - 19.06.2006	PM-514-A	RV Meteor 68/2
20.06.2006 - 01.03.2008	KPO-1001	RV L'Atalante (GEOMAR4)
02.03.2008 - 05.11.2009	KPO-1023	RV Meteor 80/1
06.11.2009 - 02.06.2011	KPO-1044	RV Maria S. Merian 18/2
03.06.2011 - 06.11.2012	KPO-1063	RV Maria S. Merian 22
07.11.2012 - 03.05.2014	KPO-1089	RV Meteor 106
04.05.2014 - 21.09.2015	KPO-1125	RV Meteor 119

Table 2.1: *Overview of equatorial moorings at 23° W. The first three mooring periods were deployed within the PIRATA program. Since 2006 the physical oceanography department of GEOMAR Helmholtz Centre for Ocean Research in Kiel operates this mooring.*

There are two very promising aspects about the equatorial 23°W mooring. First the setting of the mooring changed only slightly in the course of time producing long time series for a large depth range and now covering more than two and a half EDJ cycles. But deploying instruments does not always lead to recovering data; especially in the case of the moored profiler (see section 2.1.3). So secondly it should be noted that the fraction of successfully recovered velocity data - especially upper ocean measurements - is remarkable. In fact consecutive ADCP measurements are available for a period from early 2004 until late 2015 and a depth range of at least 300m - still continuing. All available velocity data

(from moorings and CTD/lADCP) was collected and then combined on a grid that is uniformly distanced both in space and time (see section 2.2.2 and Figures 2.1 and 2.2).

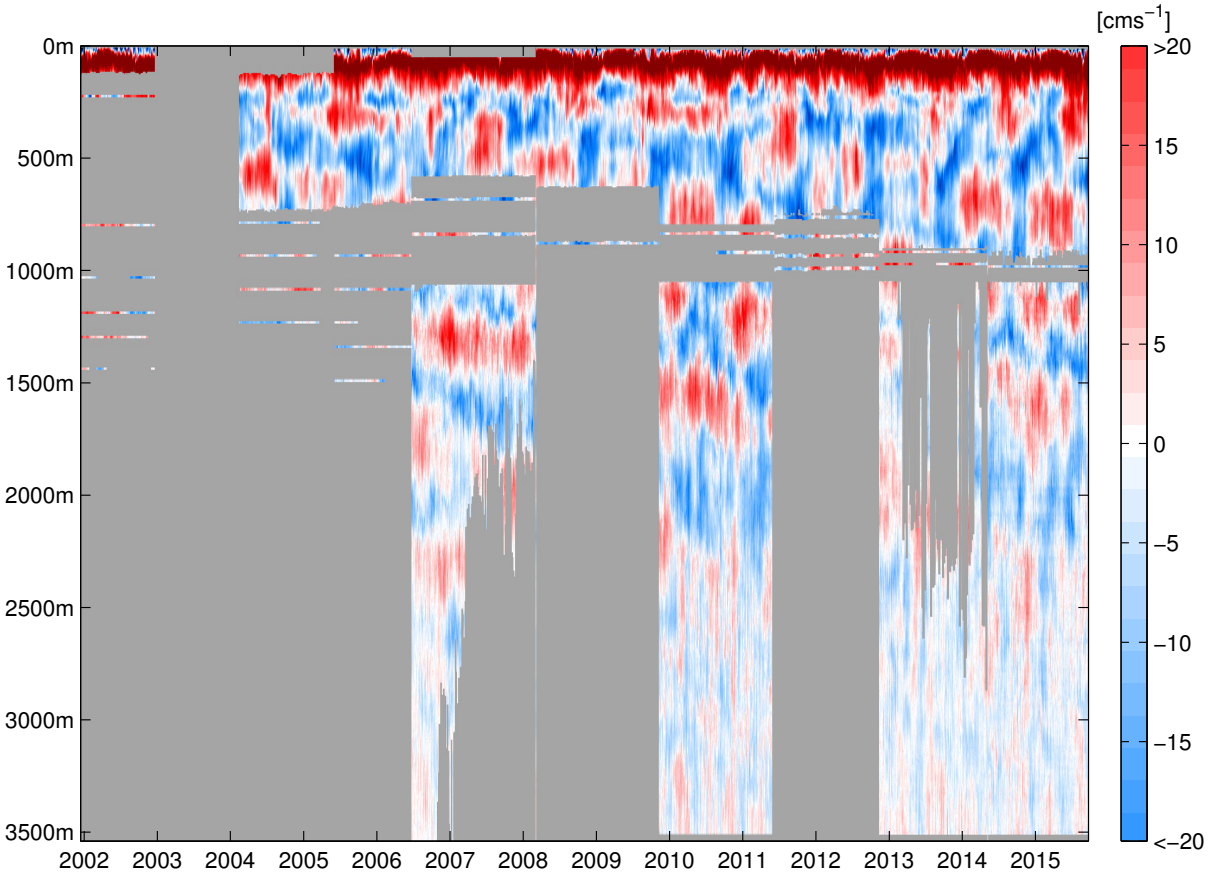

Figure 2.1: *Interpolated zonal velocity (14.12.2001 - 21.09.2015) at 23°W/Equator. Vertical resolution: 1m; temporal resolution: 12h. Higher velocities than 20 $\frac{cm}{s}$ are darkred to account for large velocities within the EUC. Grey areas represent missing data. Single point measurements are expanded to 10m width around true depth.*

2.1.1 ADCP

Acoustic Doppler Current Profilers (ADCP) are a very useful measuring instrument to collect velocity data in the upper ocean. They make use of the Doppler Effect which describes a frequency shift (Δf) of an acoustic signal (emitted frequency f_0) when colliding with and reflected by a moving object (traveling speed Δv - relative to the emitter):

$$\Delta f = \frac{\Delta v}{c} f_0$$

The ADCP periodically emits an acoustic signal with known frequency. The signal is reflected at biological particles which are purely moved by the underlying ocean velocity.

The frequency shift of the reflected signal is received from the ADCP and with the according speed of sound profile (c) it can be processed into horizontal velocity data. ADCPs are either deployed in moorings, attached to research vessels (vessel mounted (vmADCP)) or attached to CTD rosettes (lowered ADCP).

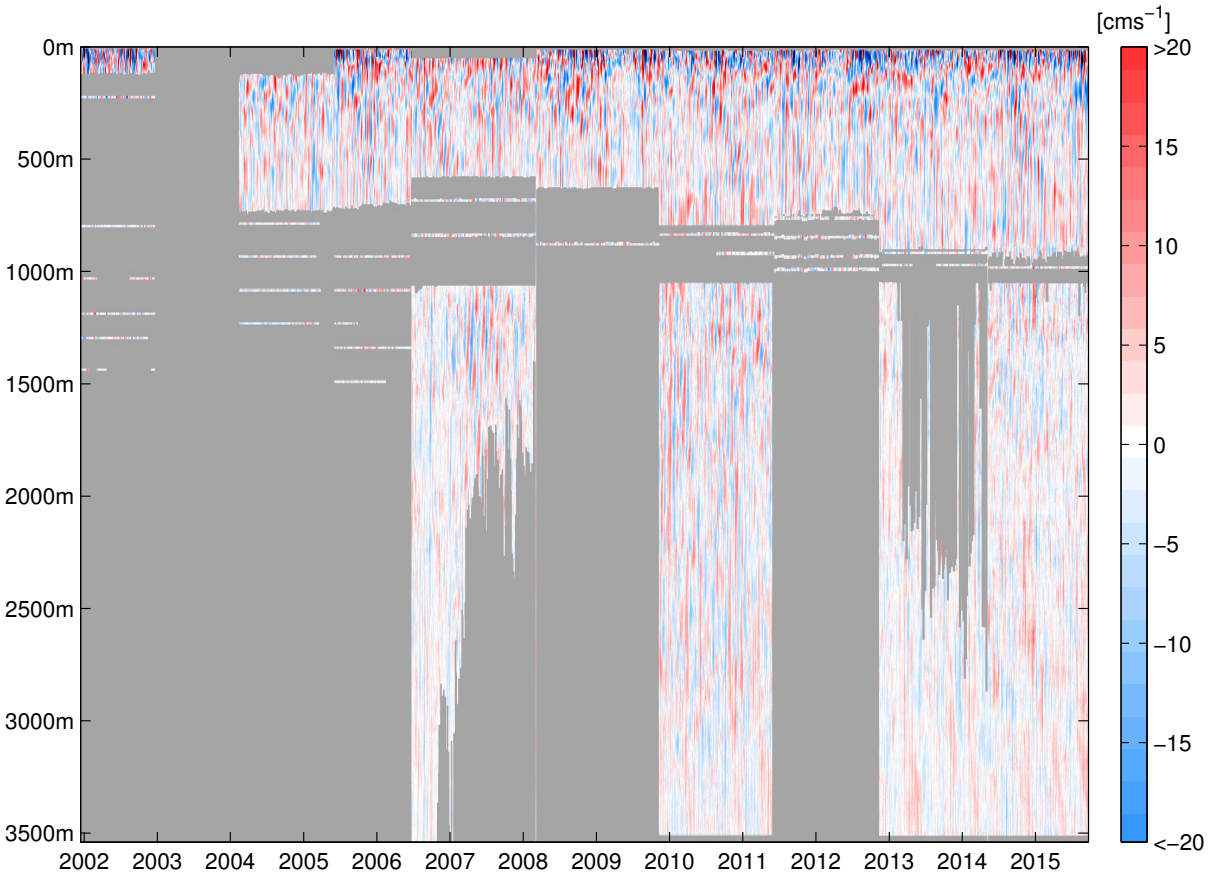

Figure 2.2: *Interpolated meridional velocity (14.12.2001 - 21.09.2015) at 23°W/Equator. Vertical resolution: 1m; temporal resolution: 12h. Grey areas represent missing data. Single point measurements are expanded to 10m width around true depth.*

The upper 600-800m of the mooring are well covered by ADCPs. Since 2008 upper ocean velocity data is merged from two opposingly orientated ADCPs at approximately 200m depth just below the Equatorial Undercurrent. The upward-looking ADCP covers the subsurface velocity field while the downward-looking ADCP reaches depths of up to 900m during the later mooring periods (see Figure 2.1). Prior to 2008 only one down-looking ADCP was deployed close to the surface and therefore not reaching the same depths as in the later mooring periods. From December 2001 until December 2002 an ADCP was deployed as part of the Prediction and Research Moored Array in the Atlantic (PIRATA). Although it only reaches about 100m depth it is included in this data set for the reason that this mooring has already been used in studies like *Bunge et al.* [2007] and furthermore

delivers single point velocity measurements between 200-1500m.

2.1.2 Single Point Measurements

Where the range of the ADCPs ends single point measurements take over. During the length of the time series different mechanical and acoustical instruments where deployed including Rotor Current Meters (RCM), Argonauts and Aquadopps to measure single depth horizontal velocities. These instruments are a very effective way to fill up the gap between the ADCP and the McLane Moored Profiler (MMP) with additional velocity data at certain depths.
Due to the vertical movement of the instruments - which is a consequence of the occasional tilt of the mooring wire - the depth of the instruments differs from the preset depth and whenever possible velocity data from single point measurements was moved from the preset depth to corrected depths by using other moored instruments which measured pressure. Even though the gap between ADCP and MMP is reducing due to better performances of the down-looking ADCP single point measurements are another important and independent source of velocity data with a high temporal resolution of 2-hourly values.

2.1.3 McLane Moored Profiler (MMP)

Since 2006 a new method of sampling deep ocean velocities and properties has been used with partial success. The McLane Moored Profiler (MMP) is part of the mooring structure ever since and supposed to record velocity data with an Acoustic Current Meter (ACM) between 1000-3500m (*Doherty et al.* [1999]). A CTD and occasionally an optode are additionally attached to the instrument to measure salinity, temperature, pressure and oxygen. In contrast to the ADCP the ACM does not make use of the Doppler shift but uses the travel time. While the ADCP relies on backscattering due to particles in the water, the MMP uses an ACM sting with four fingers (emitters) extending at a 45° angle away from a central post (receiver). On two horizontal paths and one vertically angled path a signal is constantly emitted and received by the central post. The emitted signal reaches the central post depending on the underlying ocean velocities. It arrives faster when the current flows in the same direction and vice versa. A speed of sound profile is approximated and later in the processing procedure newly calculated. Additional measurements of the three magnetic compass components and two tilt components are necessary (and performed by the MMP) to convert raw path-coordinated velocity into cartesian-coordinated east, north and vertical velocity.
Every 3-5 days (depending on the programmed setting which is based on the duration of the mooring and the battery life) the MMP is starting from the preset bottom pressure (approximately 3500dbar) and working its way up along the mooring wire with the help of a drive motor while sampling velocities, temperature, salinity and pressure. Immediately

after reaching the preset top pressure (approximately 1050dbar) the MMP samples another profile on its way down before resting for another 3-5 days. The coverage of almost 2500dbar by only one instrument is very promising but unfortunately it turns out that the MMP is not as reliable as e.g. the ADCP. The moored profiler is very sensitive to biofouling and other sources of resistance on the mooring cable. Figure 2.1 shows that from six deployments only two MMPs yielded complete data sets, two yielded partially complete data sets and another two yielded no data at all (of which one was lost during the mooring recovery and one stopped working right after being deployed). Although these are large gaps in the data set the value of the complete and even partially complete data sets is outstanding. EDJs and intraseasonal variability can now be observed and tracked into the deep ocean.

2.1.4 lADCP

Lastly, whenever available, lowered ADCP (lADCP) profiles have been added to the data set. After each mooring period CTD profiles are performed with an attached ADCP. Basically between all mooring periods one profile is added which covers the whole water column for one time step (it takes approximately 2-3 hours for a CTD profile of 3500m depth). Just as single point measurements lADCP measurements are a good way of confirming other velocity data and are included for the sake of completeness.

2.1.5 Further mooring data

For further analysis (e.g. the calculation of the Reynolds-Stress described in 2.2.6) moored velocity data from 0.75°N (KPO-1002, KPO-1024, KPO-1045) and 0.75°S (KPO-1003, KPO-1022, KPO-1043) has been assembled. Zonal and meridional velocities for both moorings are shown in Figures 2.3, 2.4 and Figures 2.5, 2.6. Table 2.2 gives an overview of the moorings, the deployment/recovery date and the recovering research cruise. These two near-equatorial moorings were operated for three consecutive mooring periods between June 2006 and June 2011. For the last mooring period a McLance Moored Profiler has been added to the mooring structures but unfortunately only the MMP south of the equator produced data. With the near-equatorial moorings meridional gradients can be calculated which is necessary for the Reynolds-Stress analysis.
The gridding and interpolation procedures are the same as for the equatorial mooring and will be explained in detail in section 2.2.2.

Time Period	Mooring	Cruise (Recovery)
0.75° N		
20.06.2006 - 29.02.2008	KPO-1002	RV L'Atalante (GEOMAR4)
06.03.2008 - 03.11.2009	KPO-1024	RV Meteor 80/1
03.11.2009 - 04.06.2011	KPO-1045	RV Maria S. Merian 18/2
0.75° S		
18.06.2006 - 04.03.2008	KPO-1003	RV L'Atalante (GEOMAR4)
04.03.2008 - 06.11.2009	KPO-1022	RV Meteor 80/1
12.11.2009 - 02.06.2011	KPO-1043	RV Maria S. Merian 18/2

Table 2.2: *Overview of moorings at 23° W / 0.75° N/S .*

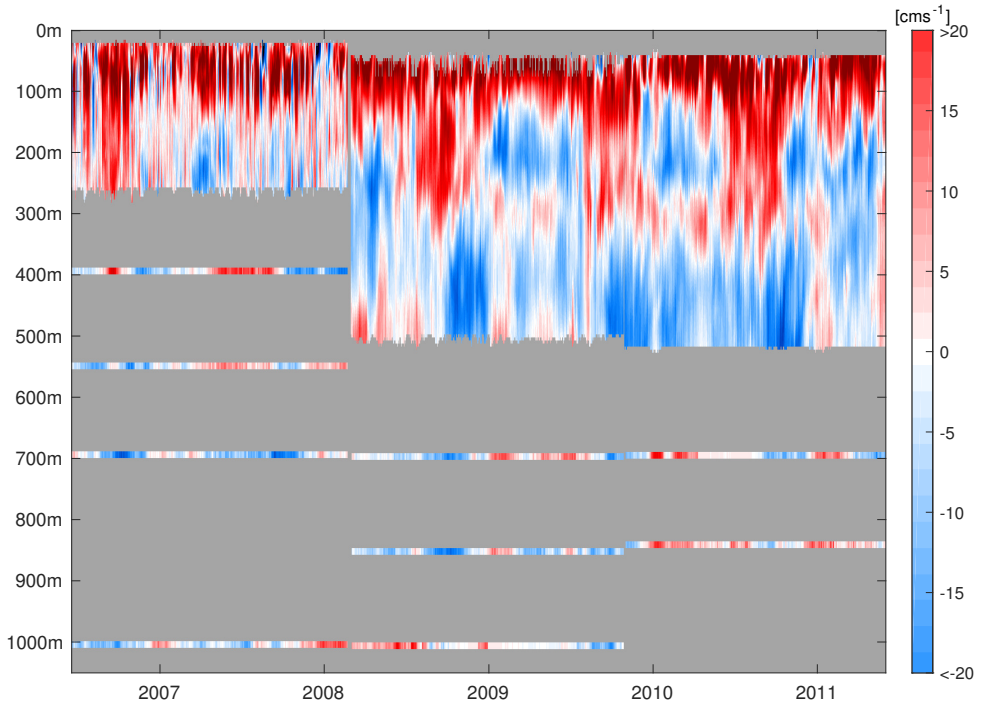

Figure 2.3: *Interpolated zonal velocity (20.06.2006 - 04.06.2011) at 0.75° N/23° W. Red colours indicate eastward flow, blue colours indicate westward flow. Grey areas represent missing measurements. Single point measurement are expanded to 10m width around nominal depth. The resolution is 1m x 12h.*

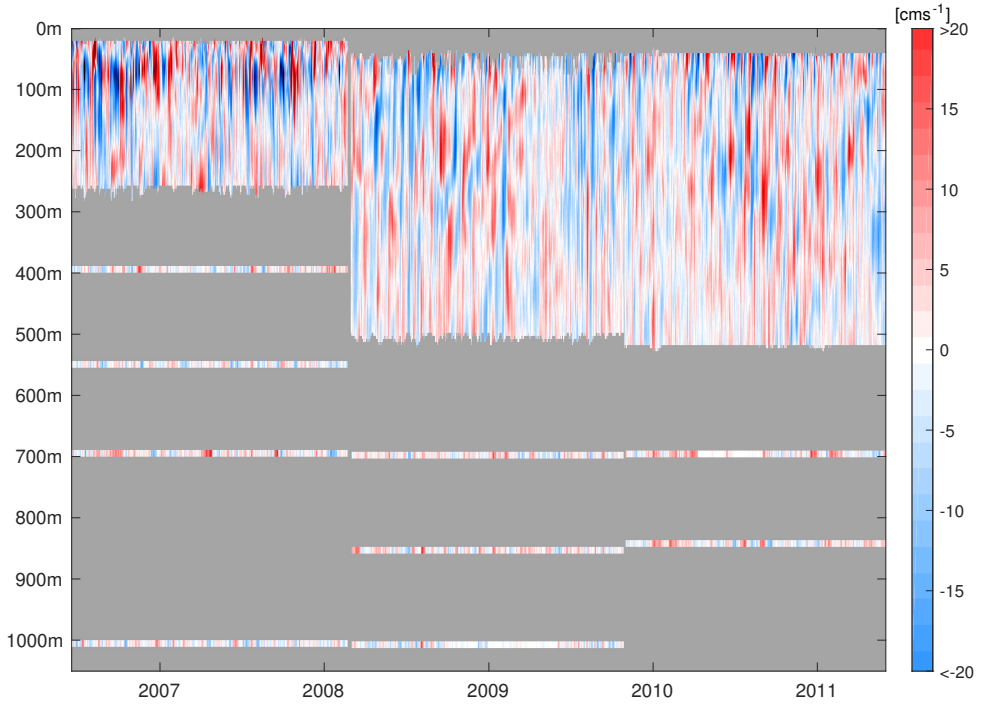

Figure 2.4: *Interpolated meridional velocity (20.06.2006 - 04.06.2011) at 0.75° N/23° W. Red colours indicate eastward flow, blue colours indicate westward flow. Grey areas represent missing measurements. Single point measurement are expanded to 10m width around nominal depth. The resolution is 1m x 12h.*

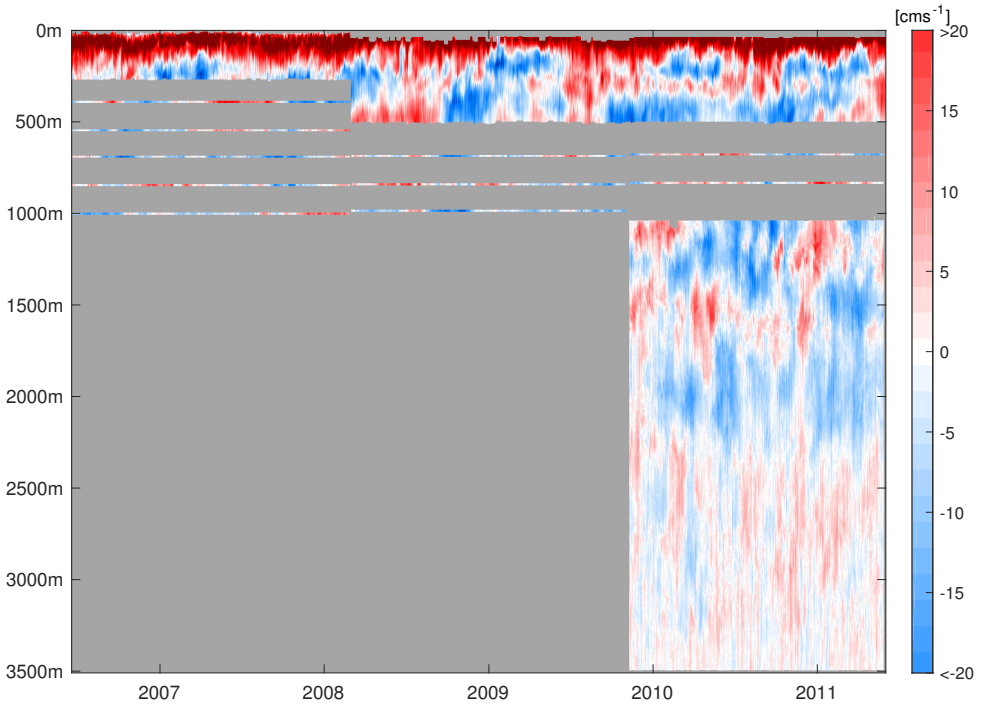

Figure 2.5: *Interpolated zonal velocity (18.06.2006 - 02.06.2011) at 0.75° S/23° W. Red colours indicate eastward flow, blue colours indicate westward flow. Grey areas represent missing measurements. Single point measurement are expanded to 10m width around nominal depth. The resolution is 1m x 12h.*

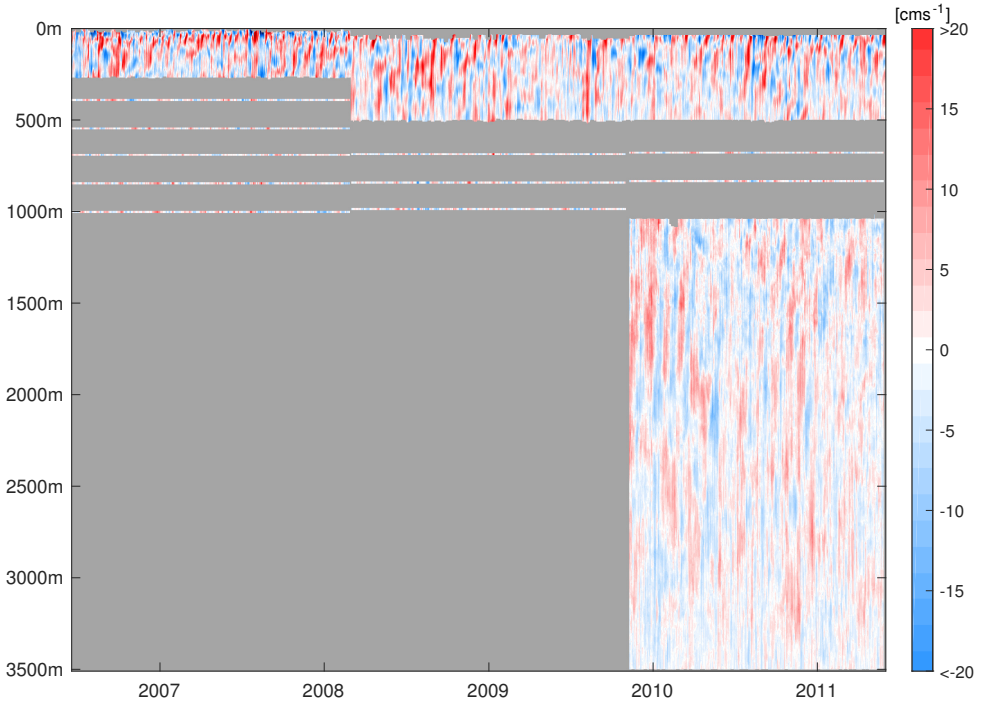

Figure 2.6: *Interpolated meridional velocity (18.06.2006 - 02.06.2011) at 0.75° S/23° W. Red colours indicate eastward flow, blue colours indicate westward flow. Grey areas represent missing measurements. Single point measurement are expanded to 10m width around nominal depth. The resolution is 1m x 12h.*

2.2 Methods

2.2.1 Processing of the MMP data

Part of this thesis and prior work was the processing of moored velocity data from the McLane Moored Profiler (MMP) and the equatorial 23°W mooring deployments KPO-1089 (2012-2014) and KPO-1125 (2014-2015). This section only gives an overview of the whole process. For a more detailed description of the processing procedure see *Didwischus* [2010].

For each vertical profile three binary files (one each for CTD data, ACM data and engineering data) is written to the flash memory card of the MMP. The CTD-files contain conductivity, temperature and pressure measurements while the ACM-files contain the two tilt components of the instrument, horizontal and vertical magnetic compass components and velocity data from the four pathways described above. The engineering files contain time information, electrical voltage and current, pressure and - if measured - oxygen data. Additionally the engineering files record the starting and end time of the sensors and the drive motor as well as the reason for finishing a profile which is important for future deployments. With an unpacking software the binary files are converted into "human readable" .TXT-files which are now processed in four major steps: first the merging of the raw data files, second the pressure gridding, third the velocity scaling and lastly the CTD conductivity calibration.

Since there are three .TXT-files for each profile (CTD, ACM and engineering data) the first step of the processing is the merging of these three .TXT-files into one .MAT-file per profile. Secondly as CTD and ACM are measuring with different sampling rates (approximately 4 and 3 Hz) it is necessary to interpolate both data sets onto the same time vector. Under the assumption of a constant sampling rate of the CTD and by including the pressure measurements of both the CTD and the engineering files a time vector is interpolated for CTD data. Consequently a starting and end point is calculated for each profile which is used to interpolate the velocity data within these points to temporally combine all three data sets. Then conductivity, temperature and pressure sensor values are calibrated by using polynomial fits from laboratory calibrations. Lastly the second step contains the compass calibration by determining the compass bias with a previously done laboratory compass spin test. It is difficult to reach precise values for the compass bias with a spin test so we chose another approach by calculating vertical mean velocities of the two horizontal components over the time series of the MMP and rotating both components. Under the assumption that the EDJs only project onto the zonal velocity the vertical mean profile of zonal velocity with the highest standard deviation over depth is chosen to be the one with the best guess of the compass bias. Similarly vertical mean profiles of meridional velocities are assumed to be rather barotropic and have a small standard deviation over depth.

The third step deals with deriving east, north and vertical velocities from raw ACM velocity path data and correcting them for the horizontal movement of the MMP during the casts. Before the correction high frequent velocity structures within one profile are filtered out. The horizontal movement of the MMP is due to the occasional tilt of the whole mooring which can be calculated from the tilt sensors and the vertical speed of the MMP. In general the corrections are lower than 1 $\frac{cm}{s}$. Furthermore the previously assumed sound speed profile is replaced by a newly calculated profile from the measured properties of the water column. After the velocity corrections the velocity data is smoothed by a low-pass filter.
In the last major step conductivity data is calibrated by using temporally and spatially close shipboard CTD measurements and single peaks have to be corrected manually by either interpolation over time with neighboring profiles or over depth with the same profile. After finishing these processing steps the data can be accessed as a .MAT-file for each vertical profile containing finally processed time, conductivity, salinity, potential temperature, pressure, velocity (zonal, meridional, vertical) and engineering data (e.g. electrical current and voltage).

2.2.2 Gridding and combination to one dataset

Since all moored velocity instruments have different temporal resolutions it is necessary to describe how they have been combined. Single point measurements generally sample horizontal velocities every two hours while moored ADCPs have a sample rate of one hour but are already merged in the processing procedure into 12-hour values. The sample rate of the MMP differs over time (depending on the mooring period) between 3 to 5 days per pair of vertical profiles. All data is low-pass filtered with a 40 hour Hamming window to account for high-frequent tidal velocities except for the MMP data, whose low sample rate makes this step unnecessary.
For the combined data set we decided on a temporal resolution of 12 hours and a vertical resolution of 1m. The single point measurements have a preset nominal depth but experience vertical movements due to the occasional tilt of the mooring which easily exceeds 1m. So, whenever possible, pressure data of other moored instruments has been used to quantify this movement and to apply a modified pressure time series to the single point measurements with varying depths for the mooring period. ADCP velocity data is usually binned into 5 or 10m values which made vertical interpolation necessary in order to achieve the aimed vertical resolution. Since CTD and ACM of the MMP have sample rates well beyond 1 Hz - while moving up and down the wire with about 45 $\frac{cm}{s}$ - velocity data has already been processed on a 1m grid.
In the temporal direction single point measurements were interpolated into 12-hour values and combined in space with ADCP data. Especially in the case of KPO-1089 and KPO-

1125 ADCP measurements reached down to depths where single point measurements were installed and supposed to measure horizontal velocities. If depths were double covered both time series were compared and always found to basically be identical. The inclusion of MMP data was more complicated. The time vector is defined by the ADCP and single point measurements. First of all for time steps where MMP velocities were measured the data was included into the 12-hourly resolved grid and the time steps between two pairing vertical profiles of MMP velocity had to be filled with empty data (NaNs). These gaps were as large as 5 days depending on the mooring. This way up- and downward profiles were placed next to each other followed by NaNs. Then whenever possible the gaps were filled by interpolation over time between values at the same depth to guarantee continuous data within the depth range of the profilers. The largest interpolated gaps were 7 days long while all larger gaps were ignored and chosen to be filled with NaNs.
All interpolation steps in the vertical and the temporal direction were compared to uninterpolated data and found to be realistic. If not further noticed the following analysis steps are based on the interpolated data sets shown in Figure 2.1 and Figure 2.2. However for some calculations the data set has been subsampled in order to reduce the computational costs.

2.2.3 Spectral Analysis

Because of the gaps in the velocity data set it was not possible to calculate the frequency spectrum of the horizontal velocity components with a common Fourier-Transformation. Instead a Lomb-Scargle periodogram has been calculated for the reason that the time series does not have to be uniformly spaced, thus allowing data gaps (*Scargle* [1982]). Unfortunately this way the spectral characteristic of depths with low data coverage is biased and has to be analysed with care. The periodogram (power spectral density (PSD)) for a given frequency ω is estimated by:

$$PSD(\omega) = \frac{1}{2}\left(\frac{[\sum_i X_i cos\omega(t_i-\tau)]^2}{\sum_i cos^2\omega(t_i-\tau)} + \frac{[\sum_i X_i sin\omega(t_i-\tau)]^2}{\sum_i sin^2\omega(t_i-\tau)}\right)$$

where X is the analysed time series of zonal/meridional velocity at the time step i, t is the time at time step i and τ the time delay at which the sinusoids would be mutually orthogonal, defined by:

$$tan(2\omega\tau) = \frac{\sum_i sin(2\omega t_i)}{\sum_i cos(2\omega t_i)}$$

With this method a Lomb-Scargle periodogram could be calculated for each depth of the zonal and meridional velocity data set with a given frequency vector that is the same as a Discrete Fourier-Transformation (DFT) would produce for a complete time series. The results are shown and described in section 3.1.

2.2.4 Intraseasonal variability

Intraseasonal variability is quantified by several methods in this work. Spectral analysis has been performed in the way described in the previous section 2.2.3 since it is the same data set with the same gaps. If not otherwise mentioned all low-pass filtering performed in this analysis has been done by applying a Hamming window which is defined as follows:

$$\omega(n) = \alpha - \beta cos(\frac{2\pi n}{N-1})$$

with $\alpha = 0.54$ and $\beta = 1 - \alpha = 0.46$. N represents the width in terms of time steps (hereafter window size) and n is a vector with size N-1.
Interpolated meridional velocities are used to construct a time series of Tropical Instability Waves activity by averaging the upper 50m and then deriving the kinetic energy v^2 at each time step. From the time series it was possible to construct a climatological cycle on the basis of almost 14 years of data (with two gaps between December 2002 - May 2005 and June 2006 - March 2008). The high resolution of two values per day makes low-pass filtering necessary in order to visualize seasonal signals in the time series. The filtering was performed as described above.
Finally harmonic cycles are fitted to the data to emphasize the annual and semi-annual signals within the climatology. The harmonic cycles are constructed by searching for the amplitude a_1 and the phase a_2 of the model function

$$x = a_1 cos(\frac{2\pi}{T}(t - a_2))$$

which minimize the covariance between the difference of this function and the original time series. A preset time vector t and a period T (e.g. 365 days for the annual harmonic cycle) have to be provided.
The characteristics of chosen Yanai Wave beams that will be analysed in this work are extracted as follows. The phase speed of a Yanai Wave is upward propagating. Within a certain time and depth window maxima (or minima) of meridional velocity are identified. Then a linear fitting model is chosen to approximate the phase propagation in a least-square sense. The resulting slope of the fit is the phase speed while the vertical distance between the phases will be the approximation of the vertical wavelength of a single beam.

2.2.5 Vertical Mode Analysis

For the vertical mode analysis the vertical mean profiles of zonal and meridional velocities have been calculated (see Figure 3.10) and subtracted from the data. Then subsampling in both time and space was necessary to keep the computational cost on a minimum while simultaneously including as much information as possible. In the end we decided on daily

values and 10m spacing in the vertical for further analysis.
With a fitting model similar to the one *Claus et al.* [2016] used it is possible to decompose the horizontal velocity components into normal modes:

$$u(z,t) = \hat{p_n}(z)\left(a_{n\omega}e^{i\omega t} + a^*_{n\omega}e^{-i\omega t}\right)$$

For a set of frequencies f (with $\omega = 2\pi f$) and a chosen range of vertical baroclinic normal modes n (for n=1,2,...,20) observational zonal and meridional velocities are fitted to vertically propagating linear waves. For each depth (z), time step (t), frequency (f) and vertical normal mode (n) complex fitting coefficients $a_{n\omega}$ and $a^*_{n\omega}$ were calculated and combined with the vertical mode structure function $\hat{p}_n(z)$. The baroclinic vertical modes are derived from a mean equatorial stratification profile at the mooring position at 23°W and normalised as follows:

$$\int_{-H}^{0} \hat{p}_n^2 dz = 1$$

Additionally the barotropic mode $\hat{p}_0(z)$ is included in the vertical structure function and normalised analogously:

$$\int_{-H}^{0} \hat{p}_0^2 dz = 1$$

Since the definition of the barotropic mode is its constant velocity with depth the equation simplifies to:

$$\hat{p}_0^2 \int_{-H}^{0} 1 dz = 1$$

$$\hat{p}_0 = \sqrt{\frac{1}{H}}$$

which becomes 1.68 $m^{-\frac{1}{2}}$ with a realistic observational depth of H=3539m. Figure 2.7 shows the vertical structure of four different vertical modes. The projected velocities $\tilde{u}$ are calculated by a normalised scalar product between the original velocities and the structure function in the form of:

$$\tilde{u} = \frac{< u, \hat{p} >}{||\hat{p}||}$$

The unit of the projected velocity is then independent of the normalisation of the structure function.
The fitting model u(z,t) is applied onto the original velocity data X(z,t) for each frequency and each vertical mode. First both the model and the data set are reshaped into one-dimensional vectors and the missing values in the velocity data are identified and not considered in the fitting process. The fitting itself is performed by a matrix division:

$$A = X(z,t)/u(z,t)$$

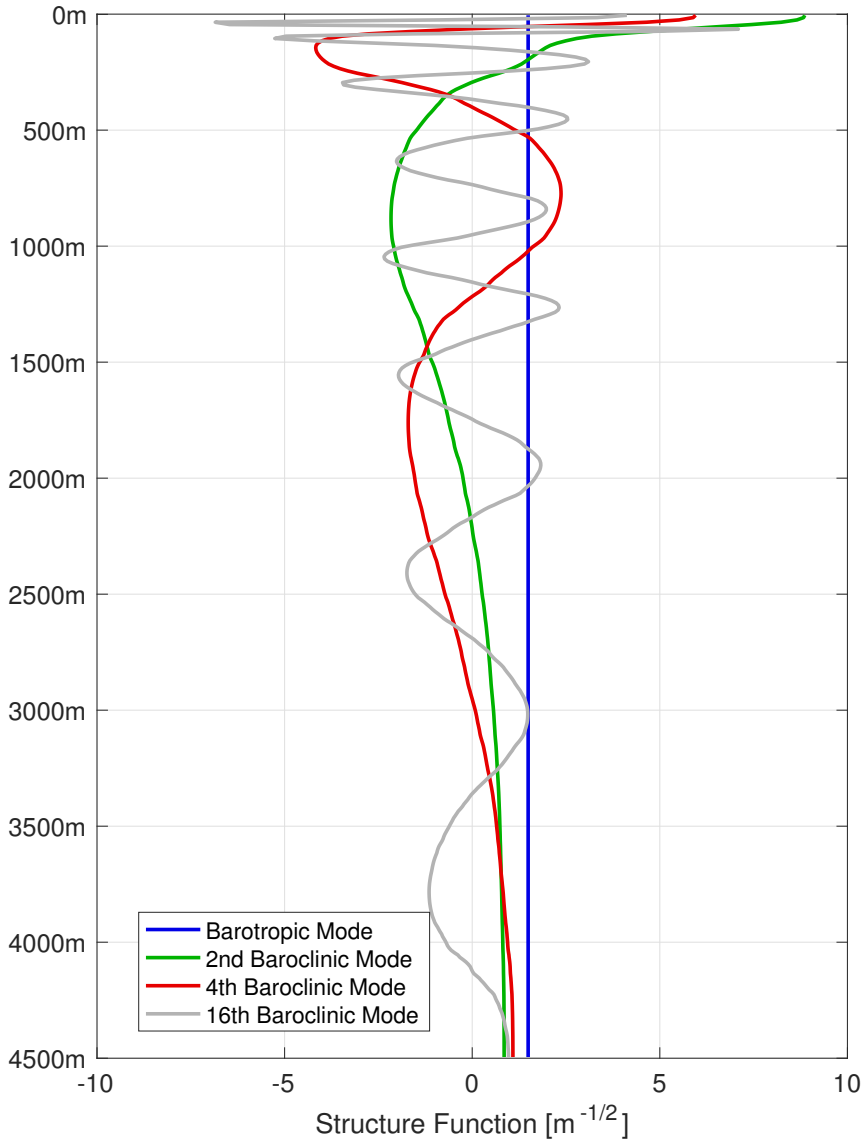

Figure 2.7: *Vertical mode structure for the barotropic mode and baroclinic modes 2, 4 and 16. The vertical modes are normalised as described in text. Here the barotropic mode for H=4500m is shown ($\hat{p}_0 = 1.49m^{-\frac{1}{2}}$).*

This way an amplitude A is calculated for each vertical mode and frequency $A(\omega, n)$ (see Figure 3.11 and 3.12). Higher amplitudes indicate that the fitting model is able to derive the actual velocity structure with a certain pair of frequency and vertical mode.
To distinguish between Rossby Waves and Yanai Waves in this vertical mode - frequency domain of the meridional velocity component the cut-off-frequency of the 1st meridional Rossby Wave can be used which is defined as follows (*Gill* [1982], pp. 445):

$$w_{cut} = \frac{1}{2}\sqrt{\frac{\beta c_m}{(2n+1)}}$$

where n is the meridional mode of the Rossby Wave, β the Coriolis parameter on an equatorial β-plane and c_m the gravity wave speed of the m-th vertical mode. w_{cut} is the maximum frequency for each vertical mode at which Rossby Waves can exist. For higher frequencies only Yanai Waves exist (and of course Kelvin Waves but they do not generate meridional velocities at the equator).
As mentioned above the dominant signals of the zonal velocity variability are on the resonance line of the gravest basin mode frequency, defined as follows (*Cane and Moore* [1981]):

$$\nu_{res} = \frac{c_m}{4L}$$

where c_m is the m-th baroclinic mode gravity wave speed and L the basin width which is approximately 55° or 6112.15km for the Equatorial Atlantic Ocean.

2.2.6 Reynolds-Stress

To derive a connection between variabilities on different time scales the Reynolds-Stress has been chosen. The original approach goes back to *Reynolds* [1895] who showed that geophysical flows can be decomposed into a mean and a fluctuating part:

$$u = \bar{u} + u'$$

The decomposition can be applied on each variable of the zonal-momentum equation which then becomes:

$$\frac{\partial \bar{u}}{\partial t} + \frac{\partial \overline{\bar{u}\bar{u}}}{\partial x} + \frac{\partial \overline{\bar{u}\bar{v}}}{\partial y} + \frac{\partial \overline{\bar{u}\bar{w}}}{\partial z} + f_* \bar{w} - f\bar{v} =$$

$$-\frac{1}{\rho_0}\frac{\partial \bar{p}}{\partial x} + \nu \nabla^2 \bar{u} - \frac{\partial \overline{u'u'}}{\partial x} - \frac{\partial \overline{u'v'}}{\partial y} - \frac{\partial \overline{u'w'}}{\partial z}$$

This is the Reynolds-averaged zonal momentum equation. Compared to the original equation the Reynolds-averaging adds three new terms on the right-hand side. These terms represent the effects of turbulent fluctuations on the mean flow and are called Reynolds-Stresses.
Since the calculation of gradients on the basis of observational data is a difficult process as there are mostly either long time series at one coordinate or horizontal sections with small time scales, we are very lucky to analyse three different moorings which were operated simultaneously over three mooring periods between 2006-2011. We will make use of the two additional moorings 0.75° north and south of the equatorial mooring to calculate the

meridional Reynolds-Stress gradient:

$$\frac{\partial \overline{u'v'}}{\partial y}$$

In our analysis the turbulent terms u' and v' are defined as the difference between the original velocity data and the "mean" velocities:

$$u' = u - \overline{u}$$

$$v' = v - \overline{v}$$

The mean velocities are derived by applying a low-pass filter (Hamming window of 70 days) on the original data to remove the influence of intraseasonal fluctuations in the mean term. A second filtering (with a 365 day Hamming window) is then performed to obtain the term:

$$\overline{u'v'}$$

This term can be calculated for each mooring at theoretically each depth which would give a set of time series for each depth. Unfortunately the first mooring period of the near-equatorial moorings reveals that the ADCP barely exceeds the lower edge of the EUC. For half of the chosen depths the analysis is only based on two mooring periods. Fortunately a single point measurement from the first mooring period could be used to generate a time series over three mooring periods at 400m depth.
The meridional gradient has been calculated from the near-equatorial terms without considering the equatorial mooring for the reason that it would not contribute to the cross-equatorial gradient. If a northern and a southern gradient would be calculated and combined the equatorial Reynolds-Stress would cancel out anyway. The meridional distance between the northern and the southern mooring (Δy) was determined to be 166.68km (1.5° latitude). Then the last step is a difference operation with discrete values rather than a differentiation:

$$\frac{-(\overline{u'v'})_n - (\overline{u'v'})_s}{\Delta y}$$

3 Results

From the different sources of data described in chapter 2 a time series for the equatorial horizontal velocities at the 23°W mooring could be constructed covering the whole water column for a period from 2001-2015. The results are merged in Figure 2.1 and Figure 2.2. The strength of the Equatorial Undercurrent between 50-200m in Figure 2.1 makes it necessary to only show velocities between $\pm 20 \frac{cm}{s}$ in order to visualize velocity structures below the EUC.

Several parts of this data set have already been analysed in earlier studies. *Brandt et al.* [2006] analysed velocity data between 2004-2005 for their study on seasonal and intraseasonal variability of the equatorial circulation. *Bunge et al.* [2008] used single point measurements between 2001-2006 to show velocity variabilities on different time scales. *Brandt et al.* [2008] studied the connection between oxygen tongues and zonal currents with ADCP data from 2004-2006. *Brandt et al.* [2011] analysed data from the 2006-2008 mooring period to quantify the impact of the EDJs on surface parameters like SST, wind and rainfall. In their analysis of the EUC *Brandt et al.* [2014] used moored velocity data from ADCP measurements between 2005-2011 and the near-equatorial moorings north and south of the equator. Recently the studies of *Claus et al.* [2016] and *Brandt et al.* [2016] focused on zonal velocity mooring data from 2004-2014. In comparison to *Claus et al.* [2016] and *Brandt et al.* [2016] one additional mooring period has been added to the data set in the present study and mooring data prior to 2004 is included in the analysis. Figure 2.1 reveals jet-like velocity structures below 200m propagating continuously downward and eventually reaching depths of about 2500m. These are the Atlantic Ocean Equatorial Deep Jets (EDJs). Besides the EUC they are the strongest zonal velocity feature at the equator with velocities of 15-20 $\frac{cm}{s}$. Between 200-2500m basically 8-10 eastward and westward propagating jets are observed at one time step indicating short vertical scales and high baroclinity. Due to the time span covered by the large amount of consecutive moorings it is possible to observe an eastward flowing jet which was excited during 2004/2005 propagating downward over time, reaching the range of single point measurements in 2011-2014 and finally entering the range of the MMP during the last mooring period. The data set is now covering almost three EDJ cycles.

Figure 2.2 shows the meridional velocity field for the period December 2001 - September 2015. In general meridional velocity variability does not have the same baroclinic structure as the zonal velocity time series. It is obvious that meridional velocity mainly varies on smaller time scales compared to the zonal velocity. The strongest velocities are reached at the near-surface caused by Tropical Instability Waves. TIWs are known to have a strong seasonal cycle. They furthermore excite beams of downward-propagating Yanai Waves. These beams reach depths of up to 1500m and propagate quite fast into

the deep ocean. Figure 2.2 shows that Yanai Waves have an upward phase propagation which implies downward energy propagation according to linear wave theory.
In the following work the intraseasonal variability from the equatorial 23°W mooring is described in several ways. First a spectral analysis of the complete data set is performed to make general statements about the observed variabilities in both horizontal velocity components. Then a focus is on the variability of Tropical Instability Waves in the surface layer. The next step is the description of single Yanai Wave beams by estimating their vertical phase speeds and vertical wavelength. Then a vertical mode analysis is performed in order to relate the variability to certain equatorial wave dynamics. Finally a connection between intraseasonal meridional variability and interannual zonal variability is quantified by using the meridional Reynolds-Stress gradients.

3.1 Spectral Analysis

To get a general overview of the variabilities in both horizontal velocity components the spectral characteristics of the two time series have been analysed. For a detailed description of the mathematical method behind this part see section 2.2.3. Because of missing data and not uniformly distanced data points a frequency spectrum has been estimated in the form of a Lomb-Scargle-Periodogram for each depth. The periodograms were then combined over depth into image plots which are shown in Figures 3.1 and 3.2. The Power Spectral Density (PSD) describes how the power of a signal is distributed over frequency. Here the power is simply the square of the analysed variable divided by the sample rate.

3.1.1 Zonal Velocity

In general zonal PSD reaches values which are one order of magnitude larger than meridional PSD suggesting that more energy is being provided by variability of zonal velocities than by meridional velocitiy variabilities.
As already mentioned in the introduction zonal velocity variability is focused on three distinct frequencies: semi-annual (180 days, 2 cycles per year), annual (365 days, 1 cycle per year) and interannual (4-5 years, 0.2-0.25 cycles per year). These three signals can be found in Figure 3.1.
The semi-annual cycle is peaking at the surface but weaker amplitudes are further apparent in the deep ocean. It is known that the semi-annual cycle is stronger in the eastern and central Atlantic Ocean compared to the western part, where the annual cycle clearly dominates. The by-far strongest signal is the annual cycle which extends from the surface to depths of approximately 1200m. Both signals are associated with annual and semi-annual wind stress forcing which excite downward propagating equatorial beams (*Brandt and Eden* [2005]). Interestingly the annual signal is strictly divided into a smaller but stronger core close to the surface and a larger but weaker signal extending from the EUC to depths between 1300-1400m; a finding that has already been described by *Brandt et al.* [2006] on the basis of an early subset of this data set. The deeper signal has another core of stronger PSD on its own located within the EUC. This pattern with a maximum above and a maximum below the mean core depth of the EUC can clearly be associated with the vertical movement of the EUC velocity core.
For depths between the ADCP range and the MMP single point measurements are not very useful for spectral analysis over such a long time since their depth occasionally varies within the same mooring period and the mooring structures changed over the whole time series. Therefore they are not yielding long time series for the same depths which is most probably the reason for vanishing signals in the PSD between 800-1100m. It can be assumed that otherwise the annual cycle signal would reach larger depths, especially

since the annual cycle signal is observed again below 1100m although it is weaker. The annual variability below the EUC is associated with the annual variability of the EIC and could also show the strong seasonal cycle of downward-propagating deep jets, although it is hard to distinguish between annual wind stress variations and the seasonal cycle of the EDJs.

On interannual time scales the Atlantic Ocean Equatorial Deep Jets produce a strong signal for periods close to 4.5 years (0.2-0.25 cycles per year). The signal is not as uniform over depth as the annual cycle which is probably due to the time span of measurements, that covers only 2-3 EDJ cycles but more than 10 annual cycles within the ADCP depth range. It can be assumed that for longer time series the interannual signal should approach the structure of the annual cycle as a relatively constant signal over depth within a distinct frequency.

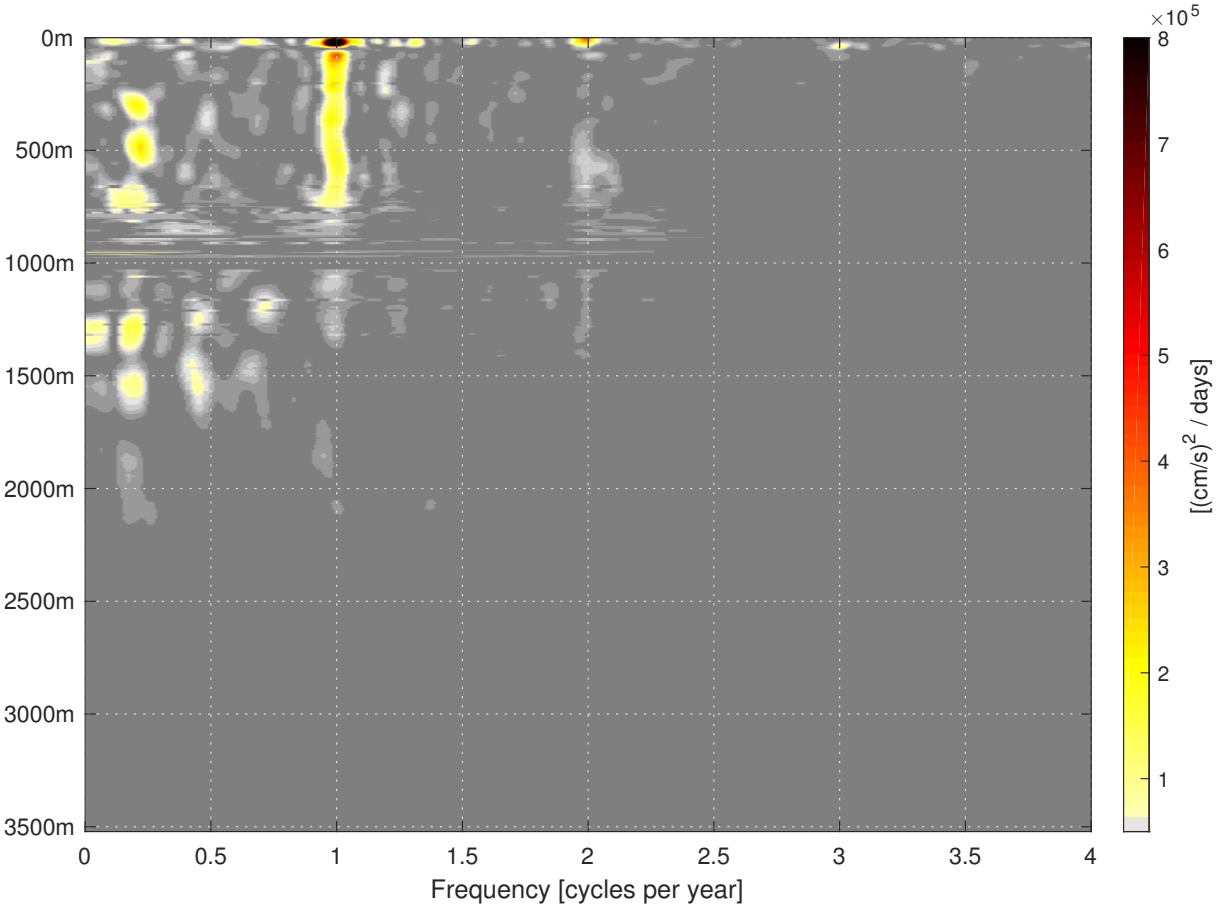

Figure 3.1: *Power Spectral Density (PSD) of zonal velocity as a function of depth and frequency. Values below 50000* $(\frac{cm}{s})^2/days$ *are excluded in order to visualize stronger signals.*

Within the MMP depth range variabilities are apparent in different frequency bands. It is unclear whether these are due to large gaps in the data or due to aliasing effects. Longer time series in these depths could give more insight in variabilities in the deep ocean but

to this point there is no evidence for other significant interannual variabilities than those associated with the Equatorial Deep Jets.
At the surface further signals within distinct frequencies are observed, e.g. for 3 cycles per year (period of approximately 120 days). Due to their limitation to the surface these signals can be associated with wind stress variabilities on these time scales but with weaker amplitudes compared to the wind-driven annual and semi-annual cycle associated with the seasonal ITCZ migration.
Power Spectral Densities for frequencies larger than 4 cycles per year and within the intraseasonal range are vanishing and cut off in order to focus on the three mentioned signals. There is some power in the intraseasonal frequency band but these are fairly weak compared to the semi-annual, annual and interannual signals.

3.1.2 Meridional Velocity

The PSD for meridional velocities is shown in Figure 3.2. In contrast to zonal velocities there are no distinct signals for certain frequencies but rather frequency domains, in which the PSD is concentrated. The highest values are reached close to the surface and are emphasized on periods between 18-40 days (9-20 cycles per year) representing the intraseasonal frequency range. These intraseasonal fluctuations close to the surface are mainly caused by Tropical Instability Waves and can propagate into the deep ocean in the form of excited Yanai Waves.
As mentioned above intraseasonal fluctuations at periods close to 15 days can also be directly forced by wind variabilities (*Athie and Marin* [2008]) but Figure 3.2 reveals more power spectral density at higher periods (lower frequencies). It seems like the thermocline layer acts as some sort of low-pass filter. Below 200-300m intraseasonal fluctuations are limited to periods higher than 25 days (or 15 cycles per year and less). Faster fluctuating signals are exclusively found near the surface and since the sample rate of the data set used for this spectral analysis is 12 hours, those signals should be well covered at least within the ADCP depth range.
Intraseasonal fluctuations with higher periods than 25 days can be observed in the deep ocean as well. As for the zonal velocities the depth range from 800-1100m is highly influenced by the lack of measurements and can be excluded in the analysis. Within the coverage of MMP measurements the highest PSD values occur between 30-40 days (9-12 cycles per year) in depths between 1100-1500m but are also observed within certain frequency bands in larger depths, like the 12 cycles per year signal between 2000-3000m. Together with the intraseasonal variability observed between 300-800m this is the Deep Equatorial Intraseasonal Variability (DEIV) which is the recently proposed fundamental source for the deep equatorial circulation including the EDJs and the EICS. Generally PSD values decrease with depth suggesting that downward propagating signals provide

their energy to other signals.

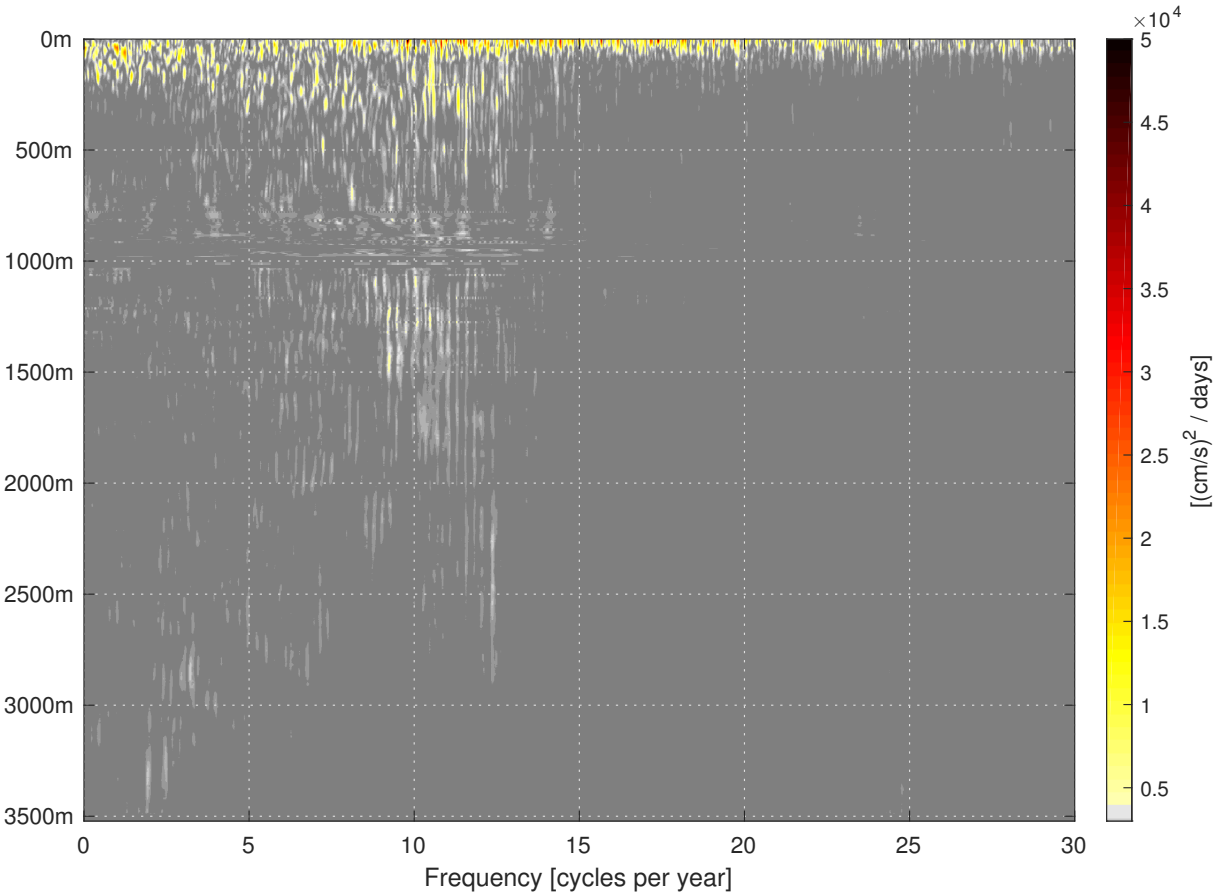

Figure 3.2: *Power Spectral Density (PSD) of meridional velocity as a function of depth and frequency. Values below 3000* $(\frac{cm}{s})^2/days$ *are excluded in order to visualize stronger signals.*

Although the PSD of meridional velocity does not show distinct signals like the zonal velocity component it still reveals elevated values for annual and interannual variabilities close to the surface indicating the annual variability of Tropical Instability Waves that is further described in the next section but also interannual variability possibly related to interannual fluctuations of the equatorial cold-tongue. Interestingly there is a weak signal in the semi-annual frequency range close to the bottom. As mentioned in the introduction this could be meridional variability due to the interaction of zonally propagating waves with bottom topography since the mid-Atlantic ridge is close to the mooring position.

3.2 Tropical Instability Waves

In the previous section it could be shown that intraseasonal variability at the equatorial 23°W mooring focuses on periods between 18-40 days and is apparent in a depth range from the surface to 2000m. A further description of the characteristics of intraseasonal variability at the equatorial 23°W mooring is needed. This section focuses on the variability of Tropical Instability Waves which are limited to the near-surface layer before the next sections emphasises on meridional velocity variability at greater depths associated with Yanai Wave dynamics and equatorial beams.

3.2.1 Time series

Figure 3.3 shows the original and the smoothed (a low-pass filter (Hamming window) of 50 days has been applied) time series of kinetic energy averaged over the first 50m. As seen in Figure 2.2 this depth range has not been covered by measurements over the whole observational period which leads to the gaps in the time series in Figure 3.3.

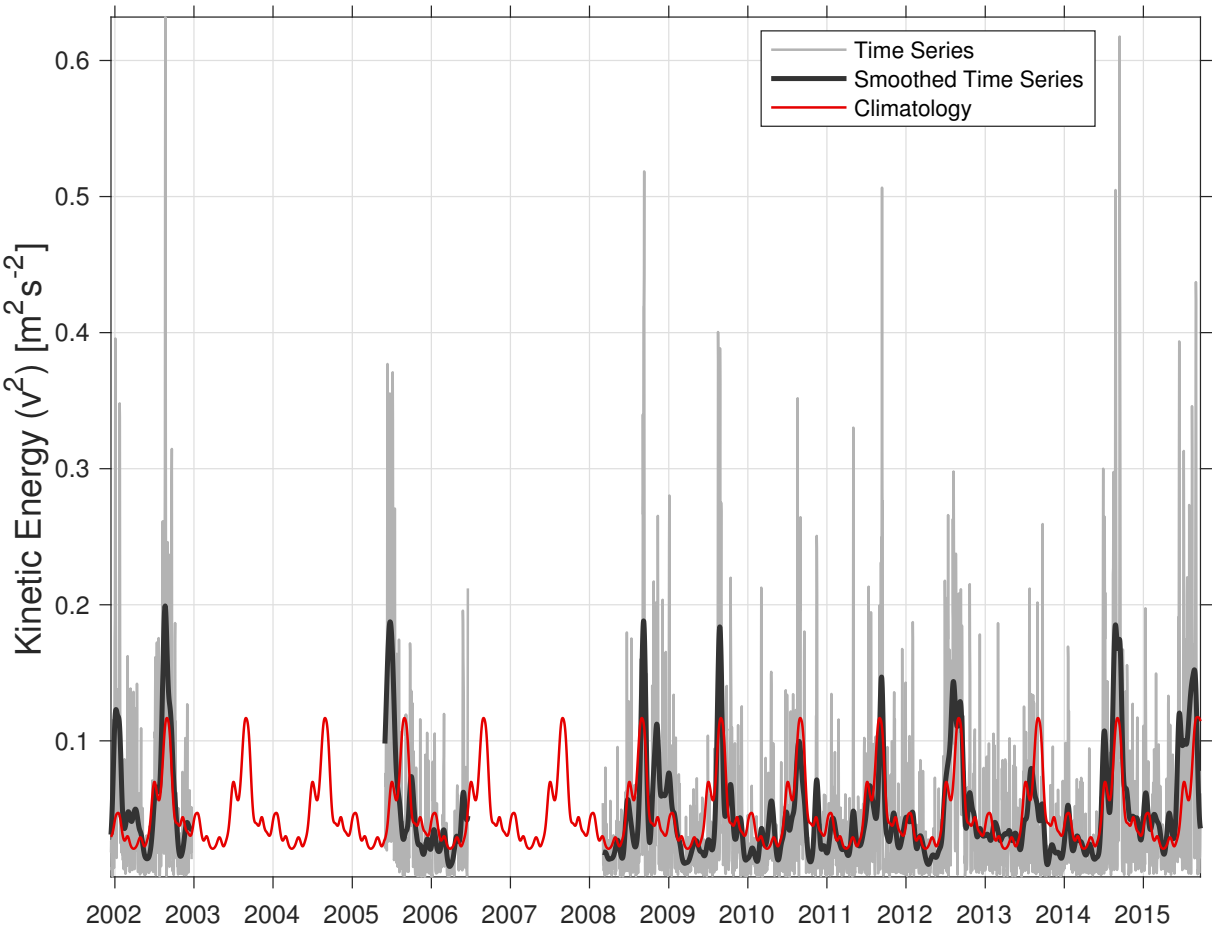

Figure 3.3: *Time series of kinetic energy (v^2) for a mean from the top 50m (grey) with an overlayed low-pass filtered (50-day Hamming window) time series (black). A climatology based on the original time series has been added (red)*

The time series reveals that the highest values occur in boreal summer. This is due to the increased strength of the south-easterly trade winds and the development of the equatorial cold tongue which leads to stronger SST fronts and stronger equatorial zonal currents. It furthermore causes stronger horizontal velocity shear and barotropic instabilities between the zonal currents. Occasionally a second maximum with weaker amplitudes is observed in boreal winter suggesting that Tropical Instability Waves vary on a semi-annual basis but this semi-annual signal seems not to be apparent in every year.
From the time series a climatology could be derived which is further described in 3.2.3. The climatology is superimposed as a red line in Figure 3.3. It matches the annual appearance of the boreal summer maximum in time but not in amplitude since the amplitude of the boreal summer maximum is subject to strong year-to-year variability.

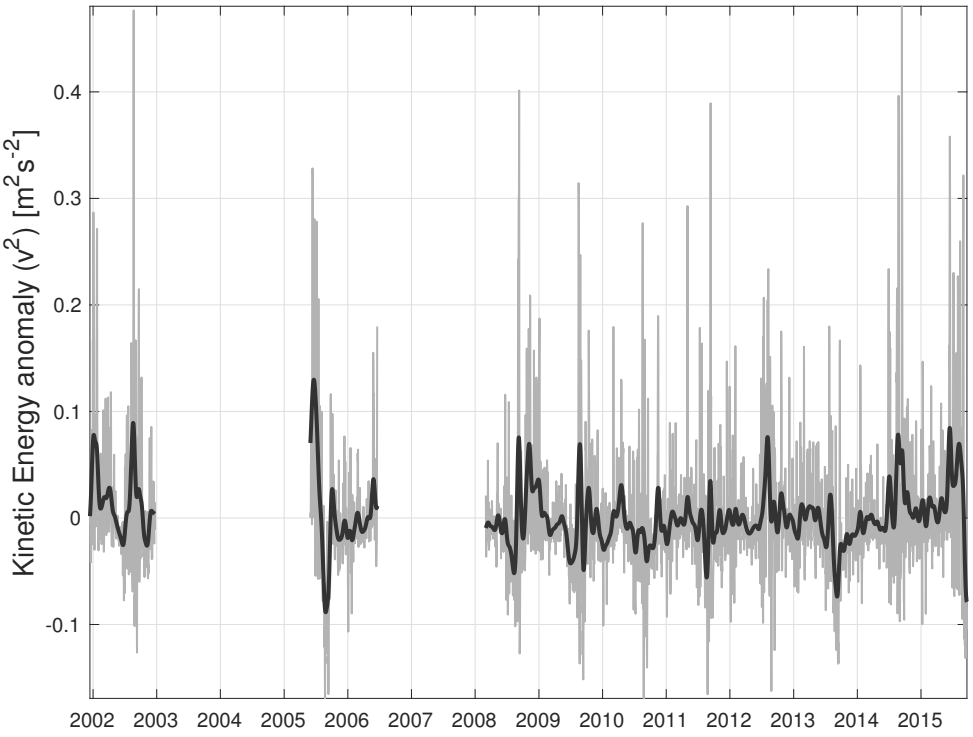

Figure 3.4: *Time series of anomalous kinetic energy (v^2) for the observation period (grey) with an overlayed low-pass filtered (50-day Hamming window) time series (black).*

On interannual time scales the equatorial cold tongue is known to vary significantly causing anomalous cold/warm events. These events most probably have an effect on the TIWs and indeed the overall trend of the TIW time series could be influenced by an underlying interannual cycle with relatively strong maxima at the beginning of the time span of measurements followed by weaker years between 2010 - 2014 and becoming larger in more recent years. For further evidence the anomalous kinetic energy has been defined as the difference between the time series and the climatological values and is shown in Figure 3.4. In general the highest anomalies are observed in boreal summer emphasizing the strong year-to-year variability that is not covered by the climatology. The largest

anomaly peaks are positive which means that the climatology underestimates these periods in the original time series. The filtered time series of anomalous kinetic energy is rather equally distributed about zero but the highest anomalies are still observed during boreal summer like in 2005 when filtered anomalies first reached positive values of more than $0.1\frac{m^2}{s^2}$ before dropping to anomalous values of almost -$0.1\frac{m^2}{s^2}$. In 2005 the equatorial cold tongue was anomalously cold which can be associated with stronger fronts and stronger Tropical Instability Wave activity. But in general the unfiltered time series shows that higher anomalies are observed in all boreal summers. It is also possible that high anomalies only represent a temporal lag of the onset of the cold tongue which could explain the sudden drop in 2005. This explanation is supported by Figure 3.3 where the climatology and the actual boreal summer maximum are shifted in the sense of an earlier than usual boreal summer maximum.

3.2.2 Spectrum

On the basis of subsampled 24-hourly meridional velocity averaged over the first 50m a frequency spectrum has been calculated (Figure 3.5). It reveals three signals that are significant on the 90%-level: an annual cycle, a semi-annual cycle and a range of signals on short time scales.

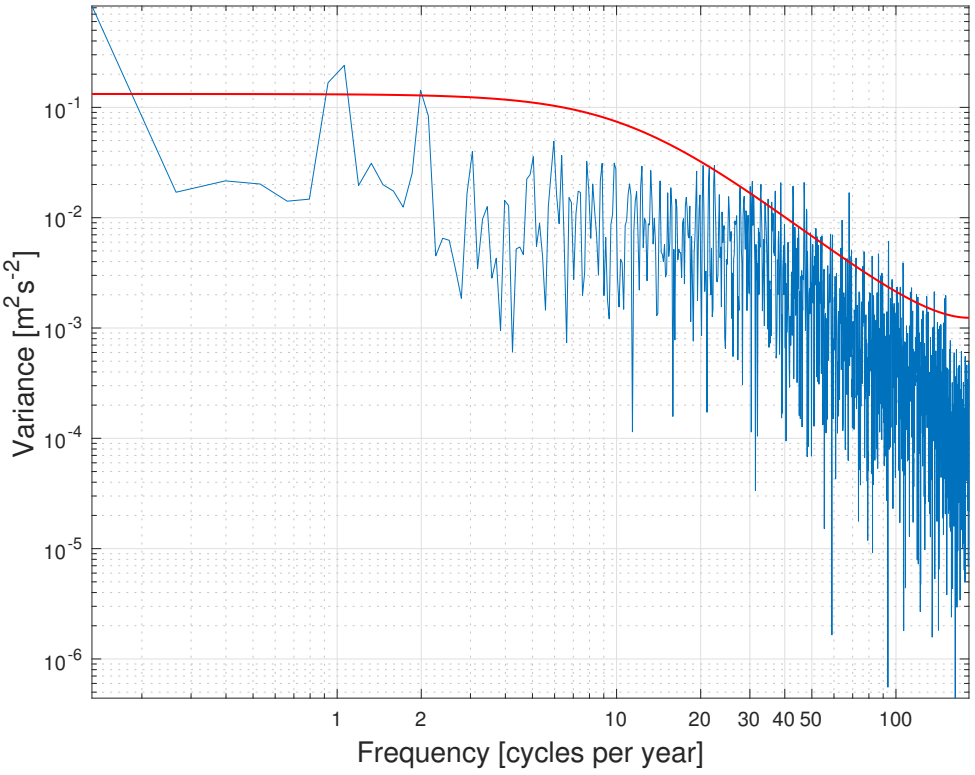

Figure 3.5: *Frequency spectrum for near-surface meridional velocities (top 50m) with the corresponding 90% significance level (red line).*

This result is consistent with the findings from the previous section. The annual cycle of meridional velocity variability within the top 50m is the strongest signal of the spectrum. The semi-annual cycle is significant on the chosen 90% significance level as well but weaker compared to the annual signal which is probably due to its rather irregular behaviour as seen in the time series (Figure 3.3). On shorter time scales the spectrum reveals a range of significant signals with frequencies higher than 20 cycles per year (or periods of 18 days and less). It is unclear whether these signals are realistic. The intraseasonal frequency range does not reveal significant variability which is not surprising but significant variability on shorter time scales is questionable when considering previous findings.

3.2.3 Climatology

In order to further analyse the seasonal structure of the intraseasonal variability Figure 3.6 shows a climatology based on the same data used for Figure 3.3.

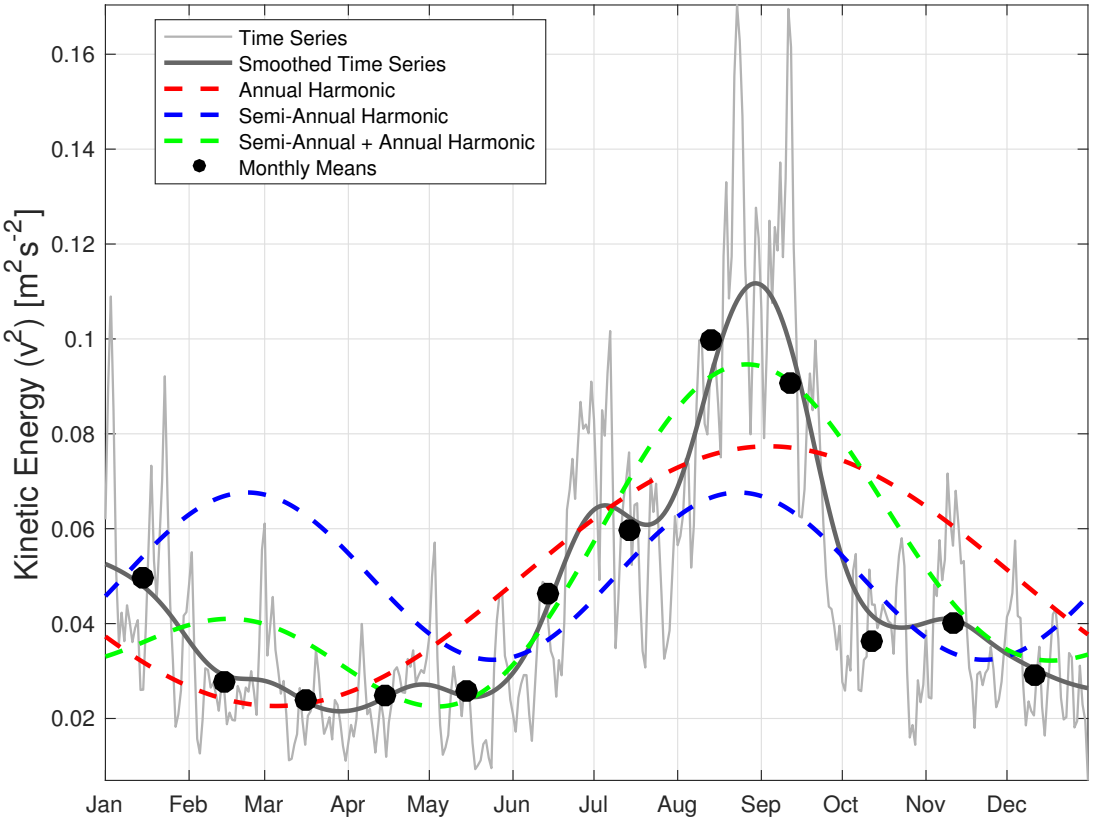

Figure 3.6: *Climatology of kinetic energy (v^2) for a mean of the top 50m (grey) with a smoothed climatology (dark-grey; 50-day low-pass filter). The black dots represent monthly mean values of the unsmoothed climatological cycle. The annual (red) and the semi-annual harmonic cycle (blue) are added as well as a combination of both (green).*

All available data has been decomposed into single years, then averaged and finally

smoothed (a low-pass filter (Hamming window) of 50 days has been applied) to derive a mean seasonal cycle. To further support the smoothed climatology monthly mean values of the unfiltered climatology have been calculated and added to Figure 3.6 which match the smoothed climatology very well. As already expected from the time series the climatology shows a distinct maximum in August/September which is right after the onset of the equatorial cold tongue in boreal summer.
The maximum reaches averaged anomalies of more than 0.1 $\frac{m^2}{s^2}$. Another but weaker maximum is observed in January with anomalous values close to 0.05 $\frac{m^2}{s^2}$. The time series revealed that this maximum is not as persistent in timing and amplitude as the stronger maximum in boreal summer but in all winters between 2010-2015 a semi-annual peak is visible although they seem relatively weak in some of these years. The semi-annual peak can be seen as a quasi-regular signal because otherwise the spectrum in Figure 3.5 would not show a significant maximum for the semi-annual period. It is possible that the migration of the ITCZ could be responsible for the weak maximum in boreal winter since this is the time, when the ITCZ is located on the equator at 23°W. Furthermore an annual and a semi-annual harmonic cycle have been fitted to the climatology. The annual harmonic (shown in red) fails to reproduce the strong maximum in boreal summer on its own although it is able to reproduce the onset while the semi-annual cycle (shown in blue) only matches the onset of the boreal summer maximum but due to its smaller amplitude can not be responsible for the observed amplitudes alone. Only the combination of the annual and the semi-annual cycle (shown in green) is able to reproduce more realistic amplitudes and the phase of the second maximum. The maximum in boreal winter could not be explained by a simple combination of both harmonic cycles indicating that there is more variability forcing this maximum.

3.3 Yanai beams

In the following section the analysis will focus on intraseasonal meridional variability below the near-surface layer and therefore out of the range of Tropical Instability Waves. Intraseasonal variability in these depths is predominantly characterised by Yanai Wave dynamics. It has to be mentioned that some caution has to be applied when analysing mooring data. The Yanai Waves that are captured by the mooring data are generated by Tropical Instability Waves close to the surface at a position westward of 23°W and likewise excited beams at the surface at 23°W are propagating away from the mooring in time and depth. The beams are propagating down and eastward while their phase propagates upward. With the mooring data used in this work no statements about the downward propagation can be made since it is simply not covered by a single mooring array. What can be seen is the upward phase propagation of the wave and the vertical wavelength which will be analysed in the following for certain beams in 2007, 2011 and 2014. As mentioned above only certain characteristics can be analysed with the present

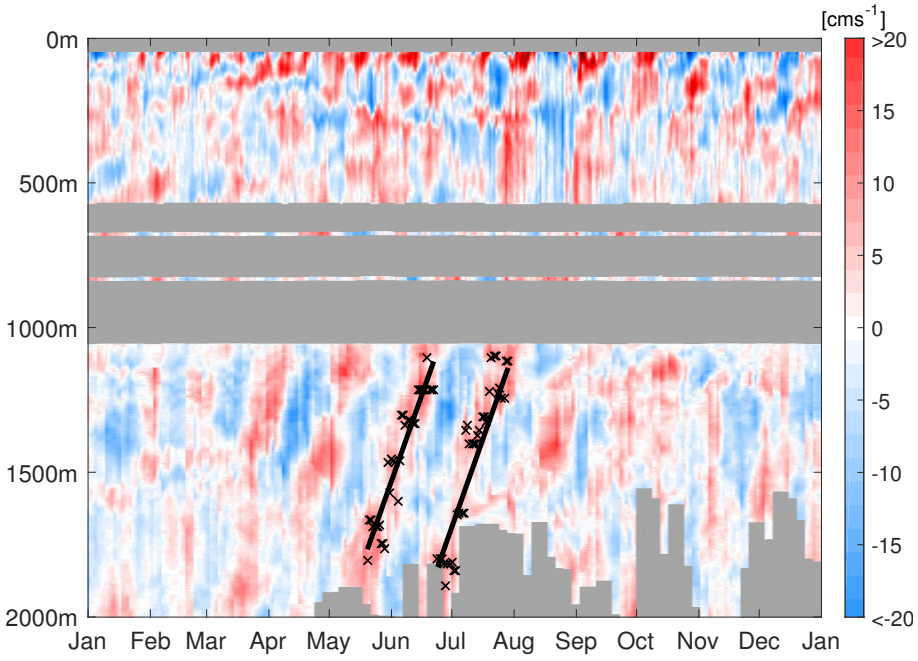

Figure 3.7: *Meridional velocity at 23° W / Equator in 2007. Vertical resolution: 1m; temporal resolution: 24h. Grey areas represent missing data. Single point measurements are expanded to 10m width around true depth. Black crosses indicate maximum velocities linearized by a least square fit (black line).*

mooring data. The vertical phase propagation is among these features. Figure 3.7 shows the meridional velocity for the year 2007 from the surface to 2000m depth.
Within a certain depth range the maximum velocities were identified at each time step and are represented by the black crosses in Figure 3.7. These data points were then approximated by a polynomial fit of the first order represented by the black line. The slope of the polynomial fit gives the vertical phase speed which are 19.67 and 23.86 $\frac{m}{day}$

for the first and second observed phase.
The chosen method is sufficient to approximate the speed of the upward phase propagation of downward propagating Yanai Waves. For a total of three especially distinct Yanai beams we performed this analysis. The next year is 2011 shown in Figure 3.8. This time it shows that the method is not always successful because the polynomial fit is very sensitive in the case of broad maximum/minimum values and no clear upward propagation. The third period in Figure 3.8 reveals not very realistic and not observed phase propagation. The two other periods reveal upward phase propagation speeds of 39.47 and 38.45 $\frac{m}{day}$. Phase speeds within a beam are quite consistent but do vary from beam to beam.

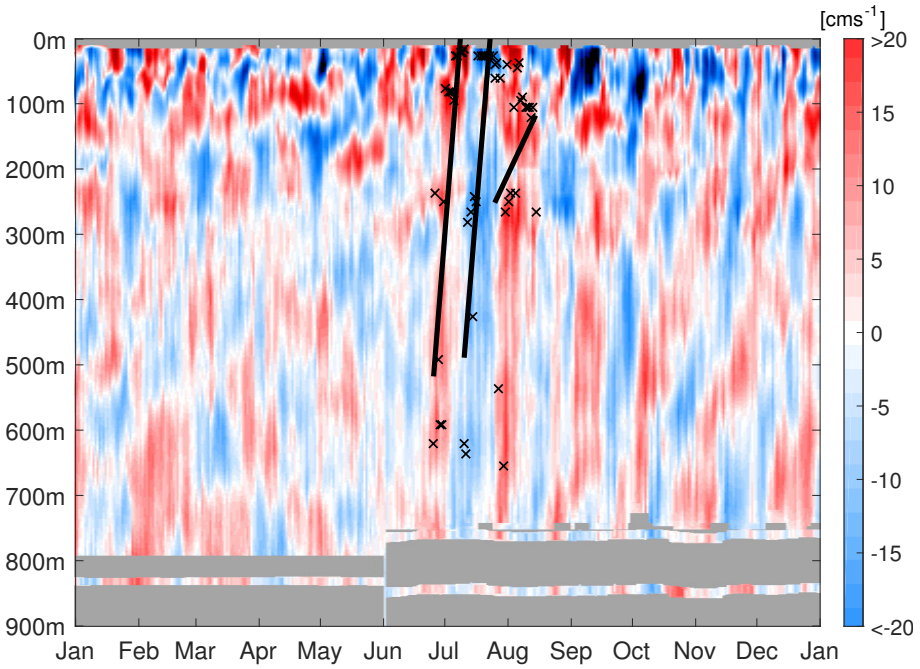

Figure 3.8: *Meridional velocity at 23°W / Equator in 2011. Vertical resolution: 1m; temporal resolution: 24h. Grey areas represent missing data. Single point measurements are expanded to 10m width around true depth. Black crosses indicate maximum/minimum velocities linearized by a least square fit (black line).*

The last period is a beam in 2014 shown in Figure 3.9. Phase speed calculations yielded values of 18.18, 16.96 and 16.42 $\frac{m}{day}$ emphasizing the consistency within a beam. The difference between certain beams and years is not clear. It is thinkable that the strength and the horizontal extent of Tropical Instability Waves at the surface sets the speed of the downward group propagation and the upward phase propagation. The analysed beams are the strongest and most significant in the data set. It is clear that the Yanai Waves in 2011 and 2014 are excited after a phase of strong TIW activity at the surface in boreal summer. In 2007 the analysed beam has already propagated down into the deep ocean and has probably been excited by the boreal summer maximum in 2006 - but as

described above west of 23°W. This fast phase propagation indicates the low baroclinity of the Yanai Waves. With the detection of certain Yanai beams and their phase speed

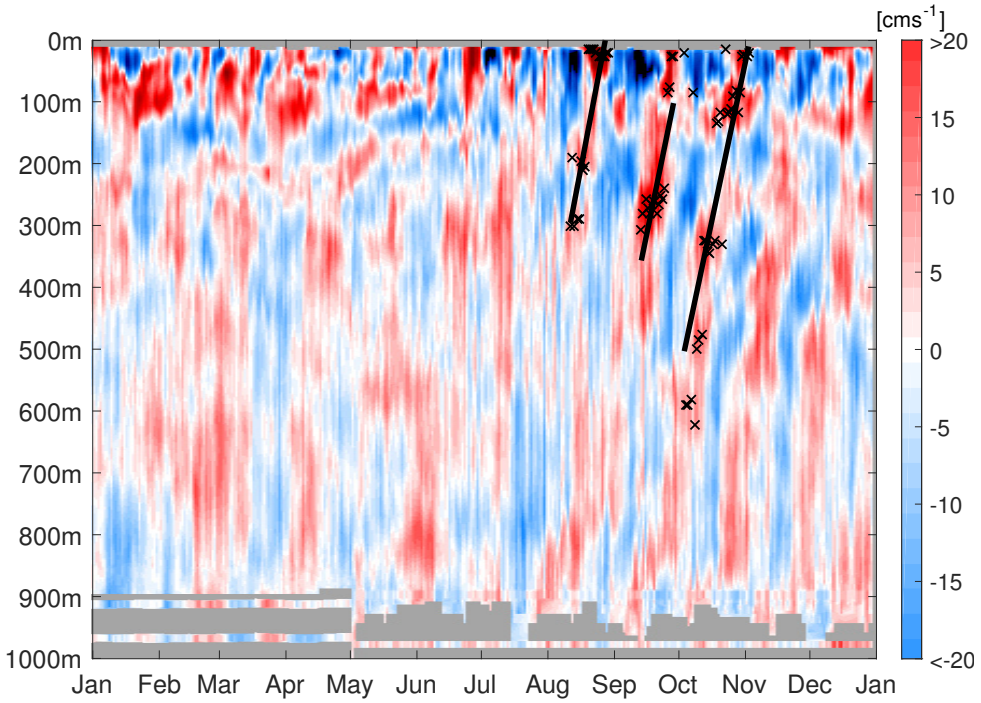

Figure 3.9: *Meridional velocity at 23° W / Equator in 2014. Vertical resolution: 1m; temporal resolution: 24h. Grey areas represent missing data. Single point measurements are expanded to 10m width around true depth. Black crosses indicate maximum velocities linearized by a least square fit (black line).*

an estimation of the vertical wavelength was done. Naturally the vertical wavelength is connected to the phase speed meaning that a faster phase propagation coincides with higher vertical scales and larger vertical wavelengths. In the case of the three chosen Yanai Wave beams from 2007, 2011 and 2014 the vertical wavelenghts have been estimated as the distance between the last maximum (minimum) within a phase and the first maximum (minimum) of the next phase. In 2007 this method yields an estimated vertical wavelength of 500-600m, wheras the two later periods give evidence for shorter vertical wavelengths of approximately 300-400m. These results are comparable to earlier studies like *Ascani et al.* [2010] who (numerically) derived a vertical wavelength of 550m for a Yanai Wave with a period of 36 days.

3.4 Vertical Mode Analysis

The main focus of this thesis is the description of intraseasonal variability in the meridional velocity data and its influence on velocity variability on longer time scales. It has already been shown in the previous sections that most energy is provided by variabilities with frequencies of 9-12 cycles per year (or periods of 30-40 days) in depths from the surface to about 2000-2500m. The next step now is to determine the source of these fluctuations which is still not fully understood. In order to associate intraseasonal variability with equatorial wave dynamics a vertical mode decomposition of the two horizontal velocity components has been performed including the first 20 baroclinic and a barotropic vertical mode by a fitting model described in section 2.2.5.

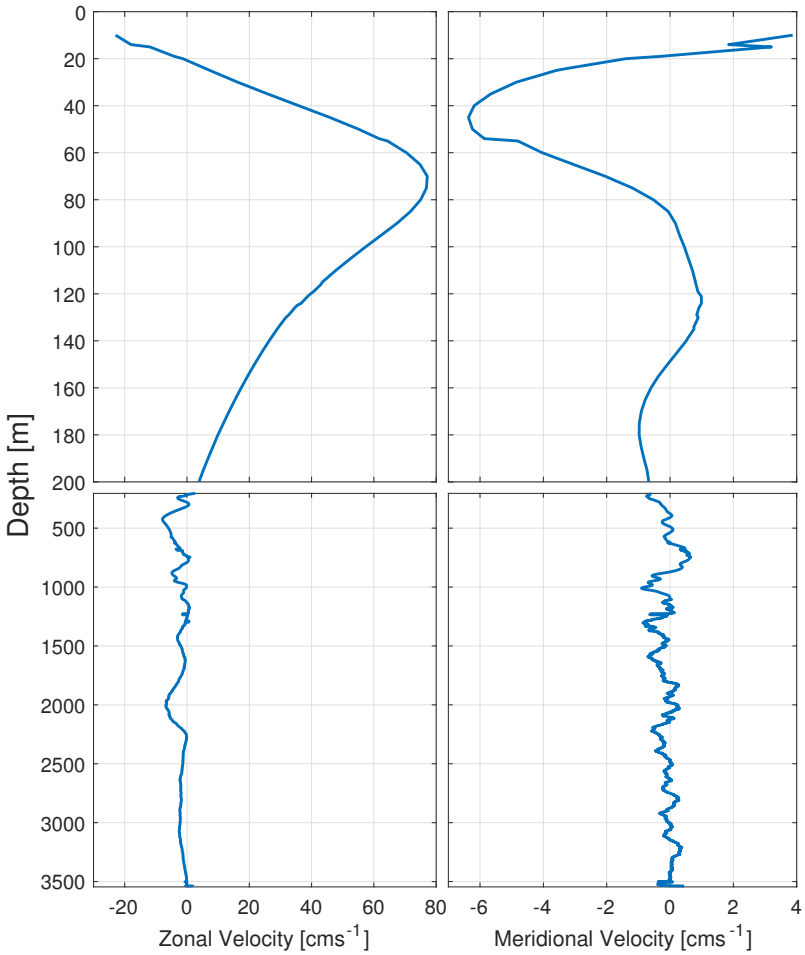

Figure 3.10: *Vertical mean profiles of zonal and meridional velocities. Note that the two upper panels are covering the upper 200m while the two bottom panels cover a depth range of 200-3500m.*

Prior to the vertical mode decomposition the temporal mean velocities have been calculated and were then subtracted at each time step from the original data set. The vertical

mean profiles are shown in Figure 3.10. Due to the lack of measurements between the ADCP range and the MMP range, mean values contain high unrealistic variability within this depth range (800-1100m) and a low-pass filter has been applied to this depth range. The permanent Equatorial Undercurrent (EUC) is observed close to the surface with a mean zonal velocity of almost 80 $\frac{cm}{s}$ as well as the Equatorial Intermediate Current (EIC) close to 500m with westward velocities of up to 10 $\frac{cm}{s}$. Below the EIC zonal mean velocities are mainly westward but not stronger than 5-10 $\frac{cm}{s}$.
Meridional velocities are about one order of magnitude smaller compared to zonal velocity values. Still Figure 3.10 reveals a persistent northward flow close to the surface and a southward flow at around 50m. This could be the footprint of a tropical cell with divergence close to the surface and convergence towards the EUC within the thermocline layer suggesting that this mooring observed the northern hemispheric tropical cell. Figure 3.10b) still reveals a lot of short scale variability throughout the whole water column. The fact that the velocity scale is shorter compared to the mean zonal velocity profile in Figure 3.10a) does not explain the variability.
After subtracting the vertical mean profiles from the original velocity data the resulting data sets were reshaped into vectors and missing values were ignored in the fitting process. For each frequency and each vertical normal mode (including the barotropic mode) the fitting model produces a vector of the same length and is then mathematically fitted to the observation vector yielding one amplitude that represents the extent of the similarity between the data structure and the structure of the current model.

3.4.1 Zonal Velocity

Figure 3.11 shows the results of the vertical mode decomposition for zonal velocities. Each value represents the magnitude of fit between the original data set and a chosen frequency and normal mode. The three distinct signals (semi-annual, annual and interannual) which have been described in the previous sections are again the most dominant signals on the frequency axis and can now be associated with corresponding baroclinic vertical modes. The annual signal is still the strongest signal in the zonal velocity data which reaches the highest amplitude for the 4th baroclinic mode. The semi-annual signal shows the highest amplitude for the 2nd baroclinic mode while the interannual EDJ signal reaches the strongest amplitude for baroclinic mode 16. Due to the fact that the original data set contains missing values the data points are not uniformly distanced and it is possible that aliasing effects occur and the originally distinct signals generate amplitudes in other baroclinic modes. This is especially the case for the annual and interannual signal. The annual signal still has high amplitudes for baroclinic mode 3 and 5 but this symmetric structure suggests aliasing effects around the "true" associated baroclinic mode. The interannual signal has been associated with different vertical modes in previous studies

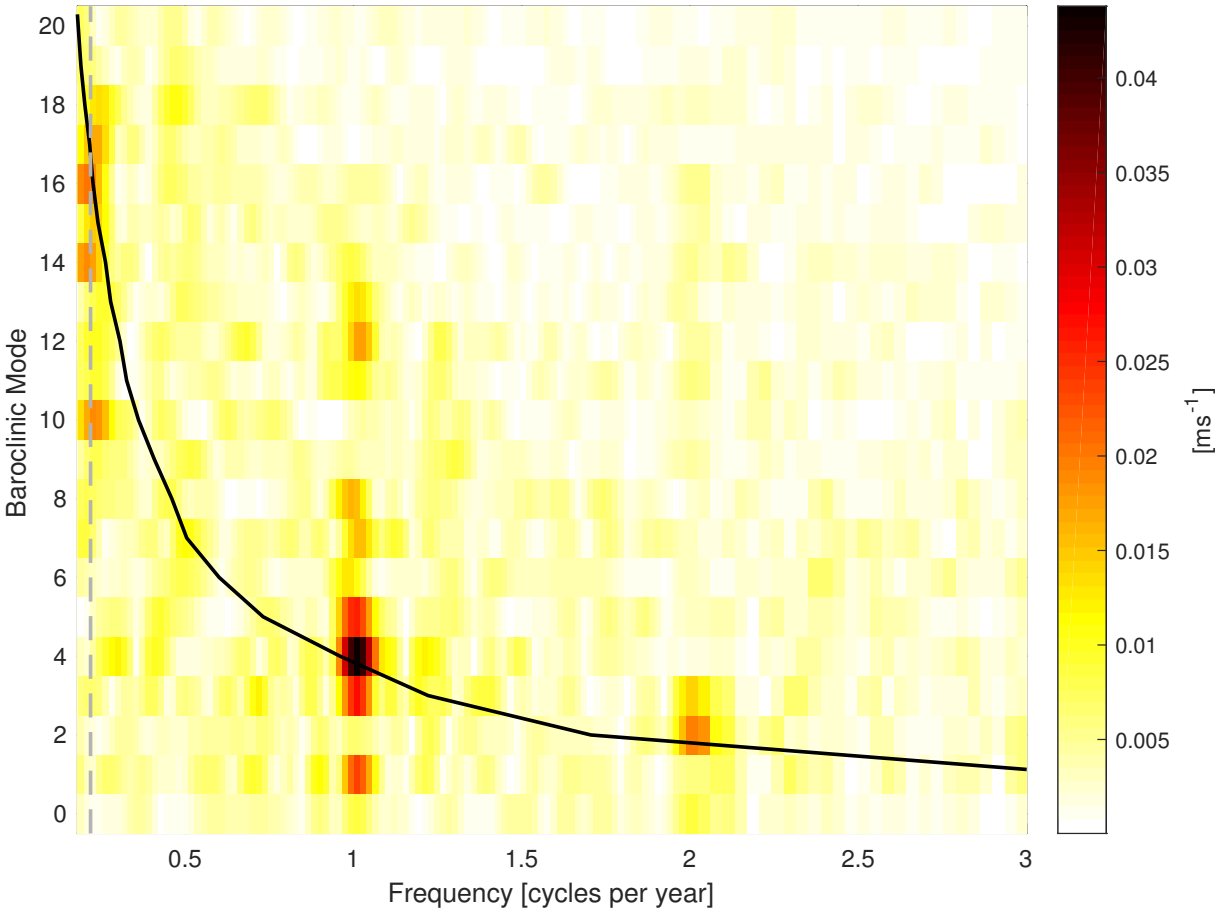

Figure 3.11: *Fitted amplitude spectrum of zonal velocity data for the first 20 vertical baroclinic modes and the barotropic mode (0th mode). The solid black line represents the gravest equatorial basin mode frequency for each mode. The grey dashed line represents the EDJ-frequency of 0.22 cycles per year (1670-day period)*

since the signal seems not be as distinct as the annual or semi-annual signal. For better visualization the 1670-day period has been added to Figure 3.11. All higher amplitudes for baroclinic mode 10, 14, 16 and 17 lie within the EDJ period. Studies often mention the similarity between the Equatorial Deep Jets and equatorial basin modes. The black line shows the gravest resonant equatorial basin mode for each baroclinic mode. As expected the line of the gravest equatorial basin mode frequency matches the vertical modes in which the energy is mostly contained. These are mode 2 for the semi-annual, mode 4 for the annual and mode 16 for the interannual cycle. The similarity between the dominant signals and the resonance line of the gravest equatorial basin mode gives evidence for their linearity.

3.4.2 Meridional Velocity

The vertical mode decomposition of meridional velocity is shown in Figure 3.12. In general amplitudes are smaller compared to those of Figure 3.11 and not focused on distinct

frequencies. Instead the amplitude spectrum reveals the highest values within a range from 9-13 cycles per year (or 28-40 days periods) and for baroclinic modes 1-10. Interestingly the barotropic mode (shown as baroclinic mode 0) contains elevated amplitudes for intraseasonal frequencies.

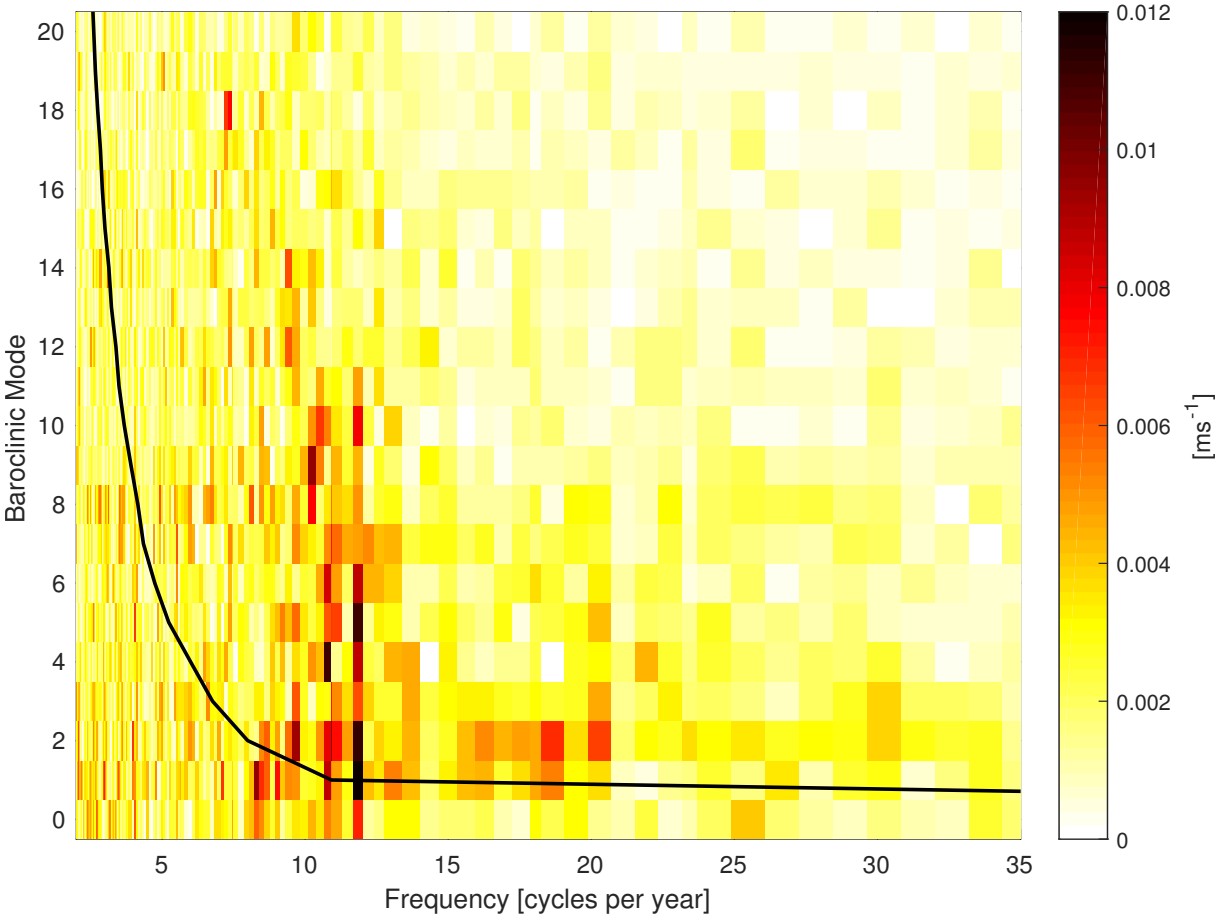

Figure 3.12: *Fitted amplitude spectrum of meridional velocity data for the first 20 vertical baroclinic modes and the barotropic mode (0th mode). The solid black line represents the cut-off frequency of the 1st meridional equatorial Rossby Wave for each baroclinic vertical mode.*

The dispersion diagram of equatorial waves (see Figure 1.4) shows that at the equator only equatorial Rossby Waves, Yanai Waves and Kelvin Waves exist within the intraseasonal frequency range. Kelvin Waves are a strictly zonal velocity feature at the equator and can therefore not be associated with meridional velocity variability. For small frequencies Rossby Waves and Yanai Waves have similar characteristics but Rossby Waves are limited to smaller frequencies due to their dispersion relation. The largest frequency (or the smallest period) for each meridional mode Rossby Wave is called the cut-off frequency which furthermore is a function of the baroclinic mode and decreases with higher vertical modes. In Figure 3.12 the solid black line represents the cut-off frequency of the 1st meridional mode Rossby Wave as a function of the baroclinic vertical mode. This line basically acts

as a boundary that allows to distinguish between amplitudes that are associated with Rossby Wave/Yanai Wave dynamics or solely Yanai Wave dynamics. Underneath and left of this line the combination of frequency and vertical mode allows equatorial Rossby Waves and Yanai Waves while above and right of this line only Yanai Waves with frequencies above the cut-off-frequency of equatorial Rossby Waves can be responsible for meridional velocity variability.

The cut-off-frequencies of the 1st meridional mode Rossby Wave for the first 10 baroclinic vertical modes and the barotropic mode are listed in Table 3.1. For the first baroclinic vertical mode the cut-off-frequency is approximately 10.92 cycles per year (or 33.44 days) which is exactly within the intraseasonal frequency range, on which we focused. It seems that the first meridional mode could be the result of both equatorial waves since it shows elevated amplitudes on both sides of the line although the highest amplitude within this mode is reached at higher frequencies within the Yanai Wave domain. There is still the possibility of Yanai Waves left of the line but it is not possible to distinguish between Rossby and Yanai Waves with our observational data set since the information of the zonal wavenumber is missing. For higher order baroclinic vertical modes Figure 3.12 clearly indicates that the strongest amplitudes are located right of the cut-off-frequency line. Generally meridional velocity variability within the intraseasonal frequency range

Baroclinic Vertical Mode	Cut-Off Frequency (cycles per year)	Cut-Off-Period (days)
0 (barotropic mode)	94.85	3.85
1	10.92	33.44
2	7.99	45.68
3	6.76	53.97
4	5.99	60.88
5	5.23	69.75
6	4.74	76.96
7	4.35	83.98
8	4.15	87.93
9	3.91	93.38
10	3.68	99.26

Table 3.1: *Cut-Off-Frequencies for the first 10 baroclinic vertical mode (and the barotropic mode) in cycles per year and the corresponding Cut-Off-Period in days. Values are rounded to the second decimal.*

can be associated with Yanai Wave dynamics at least for the 2nd baroclinic vertical mode and higher. Only the 1st baroclinic vertical mode gives evidence of a first meridional Rossby Wave forcing intraseasonal variability; but only partly since there are still high amplitudes above the cut-off-frequency and Yanai Wave dynamics can not be excluded

since they can exist on both sides of the cut-off-frequency line. The barotropic mode is of course below the cut-off-frequency since its phase velocity is as high as 186 $\frac{m}{s}$.

3.5 Reynolds-Stress

3.5.1 Step by Step

The final section of this thesis deals with the influence of the previously described intraseasonal meridional variability on interannual zonal velocity variability. In order to find a way to connect these two signals the meridional Reynolds-Stress gradient is chosen. It shows the effect of turbulent meridional fluctuations on the zonal mean flow and quantifies the connection.
On the basis of two near-equatorial moorings at ±0.75° N/S of the equator and the equatorial mooring at 23°W it is possible to calculate meridional gradients for a time period of three consecutive moorings between June 2006-June 2011. Unfortunately as can be seen in e.g. Figure 2.3 the first mooring period barely reached depths below the Equatorial Undercurrent. We chose four different depths (200m, 300m, 400m, 500m) to calculate the Reynolds-Stress terms. By including the single point measurements from the first mooring period in 400m depth, we obtain almost 5 years of horizontal velocity data for 200m and 400m while for 300m and 500m only 3 years of data is available. For better understanding each step of the analysis is shown exemplary for the 0.75°N mooring in 500m depth and explained in the following (see also section 2.2.6).

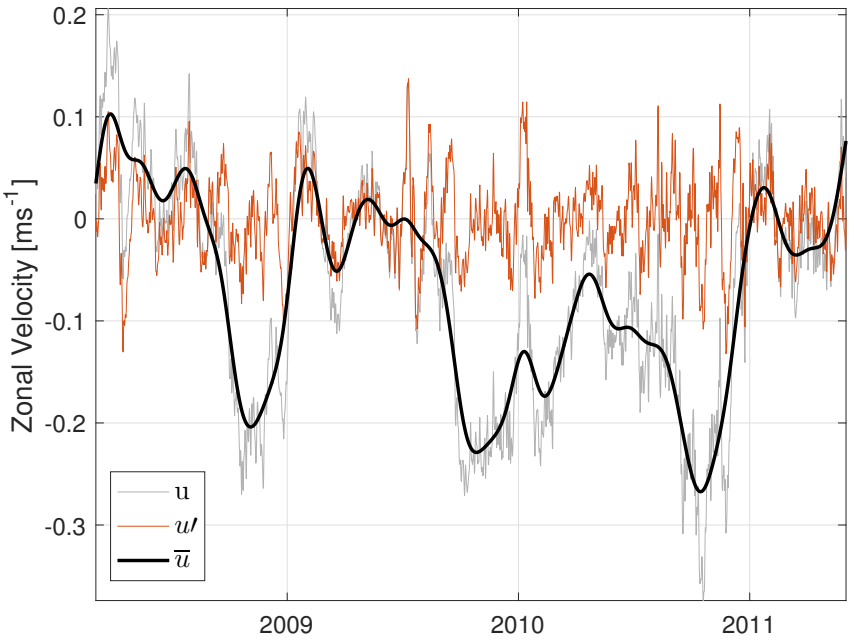

Figure 3.13: *Reynolds-Averaging of the zonal velocity component at 0.75°N/23°W in 500m. Shown are the original time series (grey), low-pass filtered time series (black) and the higher fluctuating part (red) as their difference.*

Figure 3.13 shows the different parts of the Reynolds-averaging for the zonal velocity component which separates the original velocity time series into a fluctuating part and a mean

part. This is achieved by applying a low-pass filter (70 day Hamming window) on the zonal velocity time series. The time series reveals a strong annual cycle as expected from previous findings but it also contains fluctuations on shorter time scales. The low-pass filtered time series is then subtracted from the original zonal velocity data in order to visualize the high-frequent variability of the time series. In order to calculate the meridional Reynolds-Stress gradients the meridional velocity component had to be analysed in the same way which is shown in Figure 3.14. The meridional velocity time series does not reveal a strong signal on longer time scales in 500m but varies predominantly on intraseasonal time scales as indicated by previous findings.

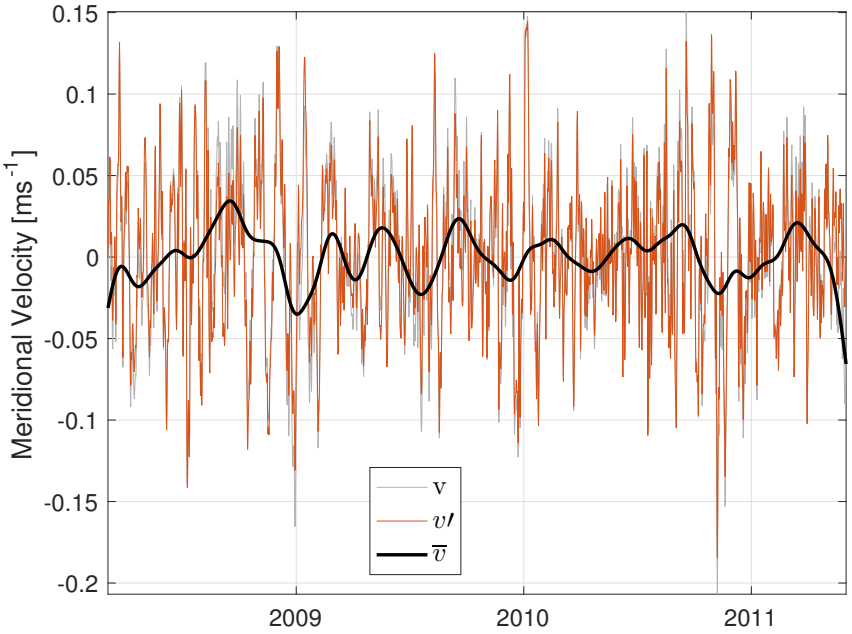

Figure 3.14: *Reynolds-Averaging of the meridional velocity component at 0.75°N/23°W in 500m. Shown are the original time series (grey), low-pass filtered time series (black) and the higher fluctuating part (red) as their difference.*

After calculating the fluctuating parts of the horizontal velocity components u' and v', both time series were combined and another low-pass filter (Hamming window of 365 days) was applied since the connection on interannual time scales is analysed and the strong seasonality disturbs this signal. The resulting time series are shown in Figure 3.15. The low-pass filtered signal is one of the three Reynolds-Stress terms that is generated when the zonal momentum equation is Reynolds-averaged. It represents the effect of high-frequent fluctuations on the mean flow and generally has small amplitudes which are nevertheless strong enough to generate changes on the low-frequent velocity variability. These steps have been calculated for each of the three moorings along 23°W at 0.75°N, the equator and 0.75°S at four different depths for a minimum of two consecutive mooring periods (or at least 3 years).

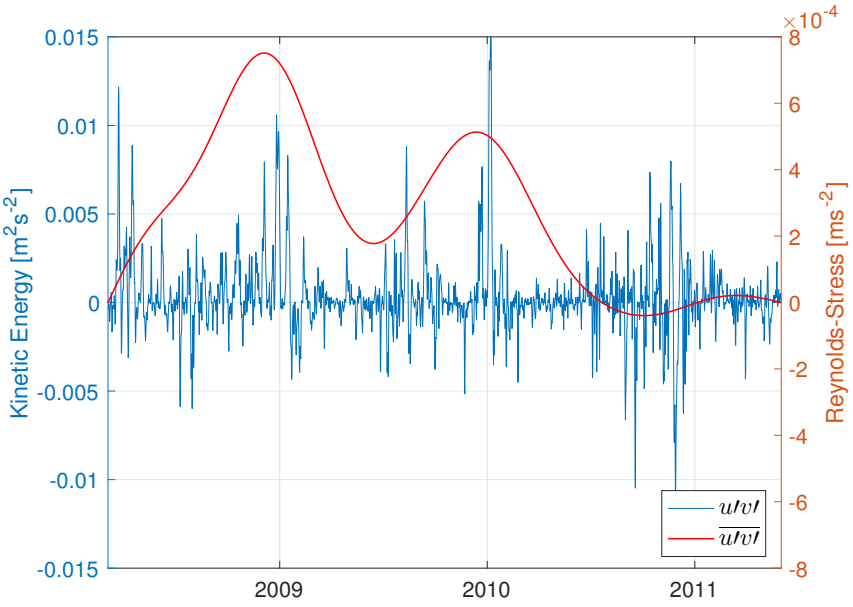

Figure 3.15: *Time series of u'v' at 0.75°N/23°W in 500m (blue) and with a low-pass filter (365 days Hamming window) applied on it (red). Note the different y-axis.*

The Reynolds-Stress terms at each mooring for a certain depth are then combined to calculate the meridional gradient of the Reynolds-Stress which is shown exemplary in Figure 3.16.

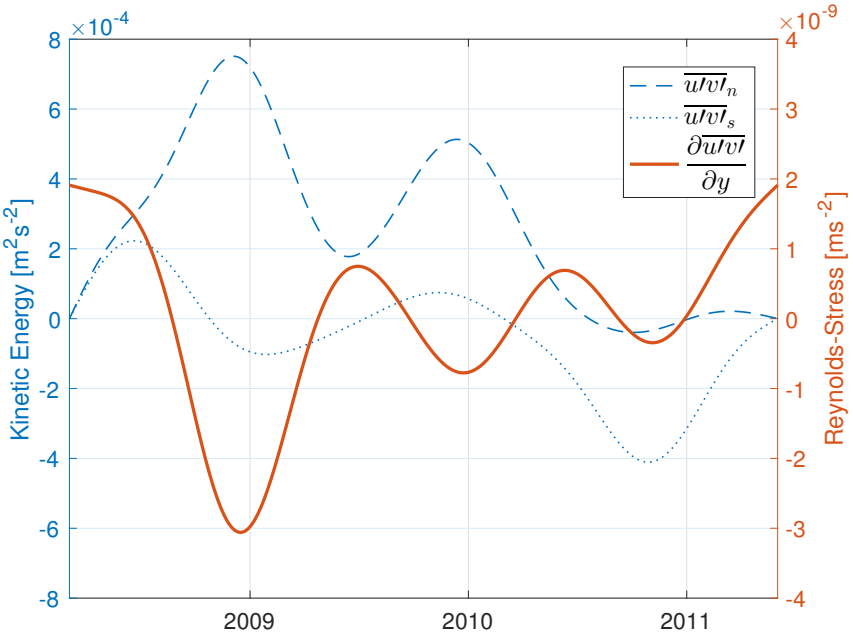

Figure 3.16: *Time series of $\overline{u'v'}$ at 0.75°N/23°W (blue dashed line) and 0.75°S/23°W (blue dotted line) together with the meridional gradient between these two time series (red solid line). Note the different y-axis.*

Due to the locations of the moorings a northern and a southern gradient can be calculated

but since the focus is on the equatorial low-frequent zonal velocity variability the cross-equatorial meridional gradient is just the cross-equatorial difference between the northern and southern Reynolds-Stress terms.

3.5.2 Reynolds-Stress gradients

Eventually the previously described steps were performed for the mentioned 4 different depths and the results are shown in Figure 3.17 and Figure 3.18.

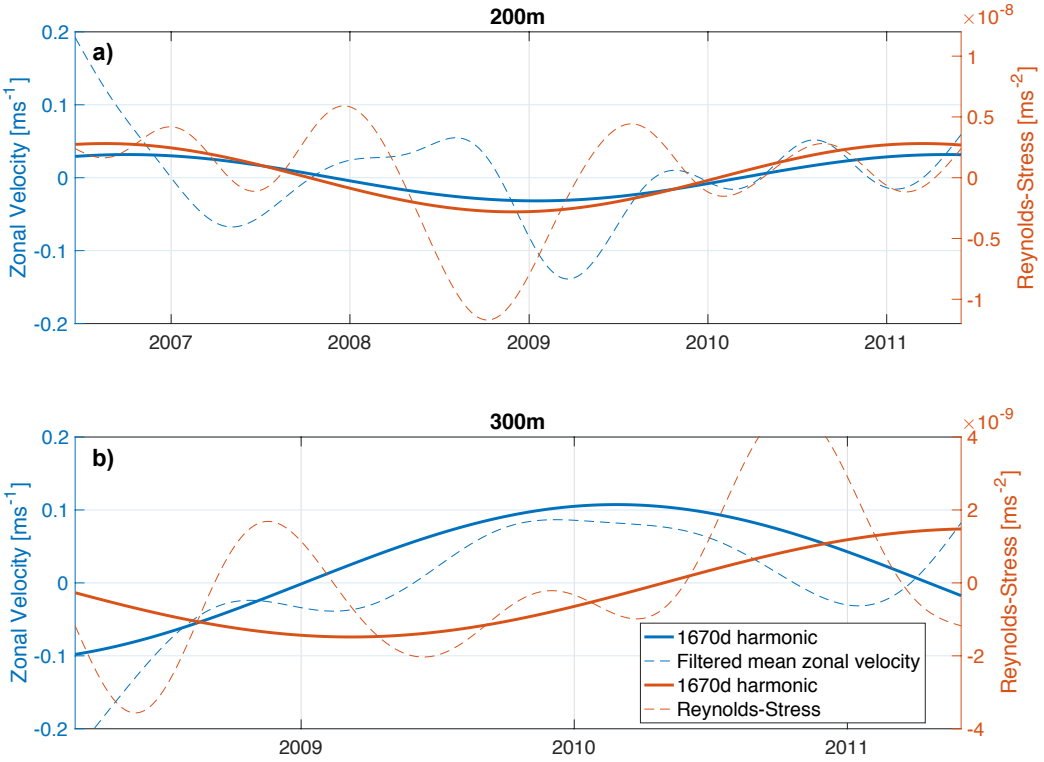

Figure 3.17: *Time series of zonal equatorial velocity (blue dashed line) and meridional Reynolds-Stress gradient between 0.75°N and 0.75°S (red dashed line) for 200m (a) and 300m (b). Both time series have been low-pass filtered (365 day Hamming window). A harmonic cycle with the EDJ-period of 1670 days has been fitted to both time series (solid lines). Note the different y-axis and time spans.*

Figure 3.17a) shows the meridional Reynolds-Stress gradient at 200m together with the zonal equatorial mean velocity at this depth. Generally both time series reveal a strong annual cycle which is why a harmonic cycle with a period of 1670 days (4.5 years; the period of the EDJs) was fitted to both time series in order to focus on the interannual connection between the two signals. It shows that for 200m depth the harmonics are only slightly shifted in the temporal direction with the meridional Reynolds-Stress gradient

advancing the zonal mean velocity by 53 days. They are almost in phase and due to the long time series which covers almost 5 years a strong correlation between high-frequent variability and low-frequent zonal velocity variability can be assumed.
In 300m depth this relation is not as clear as in 200m. Although Figure 3.17b) reveals that the overall structure of both time series seems to be related the harmonic fits do not show this connection. It is thinkable that within shorter time series the annual signal is so dominant that the harmonic cycle fits are biased and influenced by these annual peaks since the time series does not contain a whole EDJ-cycle of 4.5 years. The comparison between Figures 3.17a) and b) emphasizes the importance of long time series for the study of EDJs and points out that the harmonic fits have to be interpreted with care especially for time series with a time span lower than a full EDJ cycle.

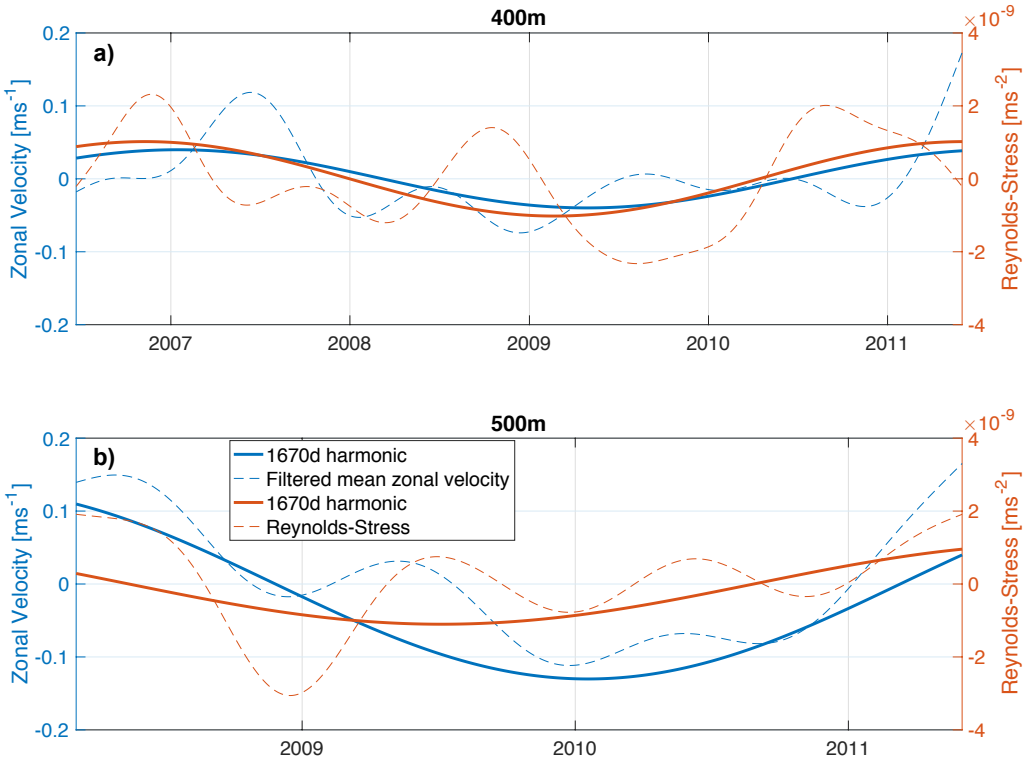

Figure 3.18: *Time series of zonal equatorial velocity (blue dashed line) and meridional Reynolds-Stress gradient between 0.75°N and 0.75°S (red dashed line) for 400m (a) and 500m (b). Both time series have been low-pass filtered (365 day Hamming window). A harmonic cycle with the EDJ-period of 1670 days has been fitted to both time series (solid lines). Note the different y-axis and time spans.*

The results for 400m and 500m are presented in Figure 3.18. Figure 3.18a) shows the calculated meridional Reynolds-Stress gradient and the corresponding mean equatorial zonal velocity (blue dashed line) for a period between 2006-2011 and at 400m depth.

Both time series are smoothed by applying a low-pass filter. Again the strong annual cycle of the zonal velocity projects onto the meridional Reynolds-Stress gradient and is visible in both the mean zonal velocity and the meridional Reynolds-Stress gradient. In order to visualize the underlying interannual structure of both time series a harmonic cycle with a period of 1670 days (the common EDJ-period) has been fitted to the data. As before the interannual Reynolds-Stress variability advances the zonal mean velocity at the equator by approximately 66 days suggesting that the zonal mean equatorial velocity is responding to the signal in the meridional Reynolds-Stress gradient. This is further indicated by the last depth that was analysed in Figure 3.18b) for 500m. Again the overall structure and the harmonic fits indicate a lagged correlation between the two time series that is influenced by strong annual variability. The time lag between the two minima of the harmonic fits is 145 days with the Reynolds-Stress advancing the zonal mean velocity on the equator.

4 Summary and Discussion

Moored equatorial velocity observations at 23°W are used to analyse the intraseasonal variability of the meridional velocity component. The time series that has been assembled for this work is an update of the data set, on which the analysis of *Claus et al.* [2016] was based on since one mooring period from May 2015 - September 2016 has been added as well as all available data from earlier mooring periods. Horizontal velocity data from December 2001 - September 2015 is now available (with some gaps) from the surface to 3500m (Figure 2.1 and Figure 2.2) covering more than 2.5 EDJ cycles.

On the basis of this outstanding data set the spectral analysis of both horizontal velocity components revealed two main aspects. First previous findings from *Brandt et al.* [2016] and *Claus et al.* [2016] are confirmed: zonal velocity variability is dominated by three distinct frequencies which are the semi-annual, annual and interannual signal (see Figure 3.1). The annual and semi-annual signals are associated with resonant equatorial basin modes (*Brandt et al.* [2016]) rather than equatorial beams that were previously used to explain the seasonal variability of the equatorial circulation (e.g. *Brandt and Eden* [2005]). The interannual signal that is associated with the period of the Equatorial Deep Jet is also consistent with studies like *Johnson and Zhang* [2003] and *Brandt et al.* [2011] which determined the period between 4-5 years. The second major result is the whole-depth spectral structure of meridional velocity variability (see Figure 3.2). It shows that close to the surface variability exists in almost all frequencies but with peaks in an intraseasonal (18-40 days) and an annual frequency range although not as distinct as in the zonal velocity component. Interestingly below the thermocline layer variability is limited to the intraseasonal frequency range and even visible within the range of the MMP below 1000m.

The present work then focused on meridional intraseasonal variability close to the surface associated with Tropical Instability Waves (TIWs). A climatology (see Figure 3.6) reveals two maxima and consequently a semi-annual cycle with a weak maximum in boreal winter and a strong maximum in boreal summer-autumn consistent with previous studies (e.g. *Grodsky et al.* [2005] and *von Schuckmann et al.* [2008]). The horizontal shear between the nSEC and the EUC produces barotropic instability (see Figure 8 of *von Schuckmann et al.* [2008]) which is strongest in boreal summer for 23°W and still present in autumn but steadily decreasing towards the beginning of the year in January-March. The study of *Grodsky et al.* [2005] is based on the first part of the same data set that was also used in this work. They were able to show that barotropic energy conversion ($-\rho\overline{u'v'}\frac{\partial U}{\partial y}$) is strongest in boreal summer-autumn (July-October) but increases again in boreal winter (December-January) (see Figure 6 of *Grodsky et al.* [2005]). This strong annual signal in TIW strength (here defined as v^2) in boreal summer is furthermore indicated by a

spectral analysis of the upper 50m (see Figure 3.5). It shows that the annual signal is the strongest and significant on the 90%-level whereas the semi-annual is also significant on this confidence-interval but only hardly. Nevertheless it can be assumed that the meridional velocity variability close to the surface undergoes a strong seasonal cycle with two maxima (a strong maximum in September-October and weaker maximum in December-January). Interannual variability of TIWs as described by *Steger and Carton* [1991] is thinkable since the boreal summer maximum is subject to strong year-to-year variability but this is not supported by the spectral analysis.

Deep ocean meridional velocity variability at the equator is associated with downward-propagating Yanai Waves (e.g. *Ascani et al.* [2015]). On the basis of almost 14 years of horizontal velocity data three especially pronounced Yanai Wave beams in 2007, 2011 and 2014 have been chosen in order to estimate the speed of the upward phase propagation and the vertical wavelength. The phase speeds are relatively constant within a single beam and reached values between 16-40 $\frac{m}{day}$ but they do differ substantially from beam to beam. Similarly the vertical wavelengths were quantified. The resulting scales of 300-600m are in agreement with findings of e.g. *Ascani et al.* [2010] who calculated a vertical wavelength of 550m for a 36-day Yanai Wave.

With a decomposition of both horizontal velocity components into vertical modes similar to *Claus et al.* [2016] previous findings of *Brandt et al.* [2008], *Brandt et al.* [2016] and *Claus et al.* [2016] were confirmed for the zonal velocity component (see Figure 3.11). It shows that zonal velocity variability is concentrated in three distinct frequencies which can be associated with certain vertical modes. The semi-annual signal is connected to the 2nd baroclinic vertical mode, the annual signal mostly projects onto the 4th baroclinic mode and the interannual EDJ signal is focused on the 16th mode. They furthermore are located on the resonance line of the equatorial basin mode emphasising their linear behaviour. Additionally the meridional velocity component has been decomposed as well (see Figure 3.12). Most energy is located in the intraseasonal frequency range and between the barotropic and the 10th baroclinic mode. In order to make statements about the source of equatorial meridional velocity variability the mode spectrum is divided by the cut-off frequency of the first meridional equatorial Rossby Wave. This line separates frequency-mode combinations which are associated with Yanai Wave or Rossby Wave dynamics and frequency-mode combinations which can only be associated with Yanai Wave dynamics (see the dispersion diagram in Figure 1.4). This method reveals that most of the energy is located above the cut-off frequency and must therefore be forced by Yanai Waves although there is also energy in the barotropic and the first baroclinic mode which could also be subject to Rossby Waves dynamics but of course also Yanai Waves since they are not limited to certain frequencies.

Lastly this work is using two additional moorings 0.75° north and south of the equator to confirm results from *Ascani et al.* [2015] who numerically showed that the Equatorial

Deep Jets are maintained by the Deep Equatorial Intraseasonal Variability. In their study intraseasonal Yanai Waves interact non-linearly via the meridional advection term of zonal momentum equation. Here we show that the meridional Reynolds-Stress gradient is capable of delivering similar results. In four depths (100m, 200m, 300m, 400m) the meridional Reynolds-Stress gradient is calculated. The Reynolds-Stress gives evidence for the connection between turbulent fluctuations (like the intraseasonal meridional variability) and low-frequent mean zonal flows (like the interannual EDJs). Figure 3.17 and Figure 3.18 show that a correlation between the Reynolds-Stress gradient and the equatorial zonal mean flow in almost each chosen depth is apparent when an interannual harmonic fit is applied. In all cases the meridional Reynolds-Stress gradient advancess the equatorial zonal mean flow although it has to be mentioned that the harmonic fits highly depend on the annual signals of both terms and since two of the chosen depths are based on time series with only three years of data the confidence of this time lag is questionable. Furthermore the values obtained by our analysis are lower compared to model results which can be associated with the choice of the lateral mixing of momentum usually set to 300 $m^2 s^{-1}$ (M. Claus, personal communication).
The overall forcing mechanism can be explained as follows. In general a cross-equatorial eddy that is symmetric about the equator is unable to flux momentum (Figure 4.1).

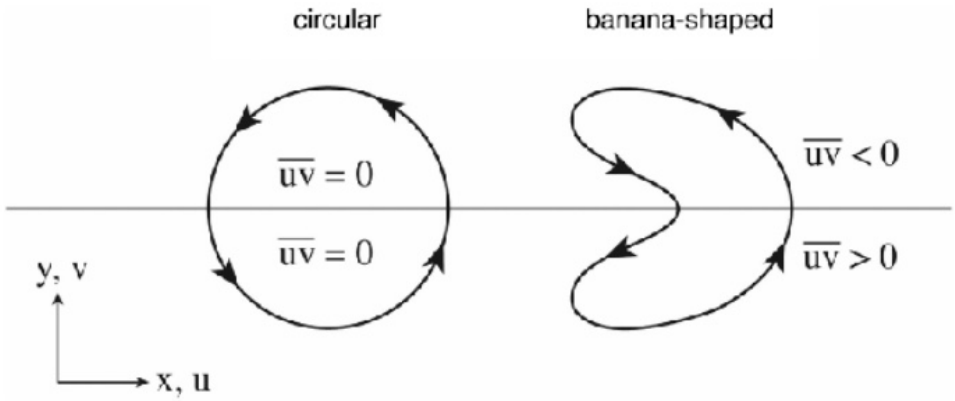

Figure 4.1: *Circular eddies are unable to generate meridional transfer of momentum whereas "banana-shaped" eddies are able to generate a meridional transfer of momentum towards the midline if they exhibit a "banana-shape" about the midline. Taken from Marshall and Plumb [2008].*

We assume a barotropic Yanai wave which initially has a symmetric velocity structure across the equator throughout the whole water column. This field is disturbed in the vertical by the zonal jets in the deep ocean forming a so-called banana-shaped eddy. Depending on the direction of the jet the eddy is deformed towards the east or the west. Considering the new "banana-shape" of the horizontal velocity field a meridional transfer of zonal momentum towards the equator is possible on both sides. This mechanism is

thought to maintain the equatorial deep jets but the initial forcing of the EDJs is till unclear.

To our knowledge this is the first time the connection between intraseasonal variability and the maintenance of the EDJs could be shown on the basis of observational data.

5 Outlook

The work that has been done in this thesis will be continued and expanded. In September 2016 the research cruise RV Meteor 130 recovered another equatorial mooring at 23°W. This mooring yielded almost complete data within the ADCP range and - like the previous mooring - within the MMP range as well. It seems like this mooring instrument stabilized in recent mooring periods. This velocity data of the recently recovered mooring is going to be included in the near future and results like the general time series, the spectral analysis, characteristics of Tropical Instability Waves and the vertical mode decomposition are going to be updated. More data is likely to further sharpen the image of meridional velocity variability in the intraseasonal domain. Longer time series of zonal and meridional velocity will also result in a better understanding of the characteristics of the Equatorial Deep Jets (EDJs) in the deep ocean and the Tropical Instability Waves (TIWs) close to the surface.

The Reynolds-Stress divergence could only be calculated because of available mooring data north and south of the equatorial mooring. Unfortunately these near-equatorial moorings were only operated for three mooring periods until June 2011. A long time cross-equatorial meridional mooring array is necessary to quantify the connection between the Reynolds-Stress divergence and the zonal equatorial mean velocity more accurately since the present data covers maximum 5 years of consecutive measurements (for some depths only 3 years). With the good performance of modern ADCPs the analysis could be expanded to larger depths than 500m.

The next steps are the analysis of the meridional Reynolds-Stress gradients for depths within the EUC since it is thinkable that the EUC can be similarly maintained by intraseasonal variability as the EDJs. This would mean that the EUC is partly providing energy for its own maintenance since the shear between the EUC and the nSEC generates barotropic instabilites which further excite intraseasonal variability. This will be further analysed on the basis of the presented observational data set.

Another interesting field of research would be the estimation of the zonal wavenumber by considering an equatorial mooring at 21.5°W which was installed for a period between 2006-2008 (see Figure 5.1). Since Yanai Waves are propagating down- and eastward another mooring at the same latitude and a more eastward position can be used to approximate the zonal wavenumber for beams towards the end of the time series, when both moorings show distinct Yanai Wave dynamics.

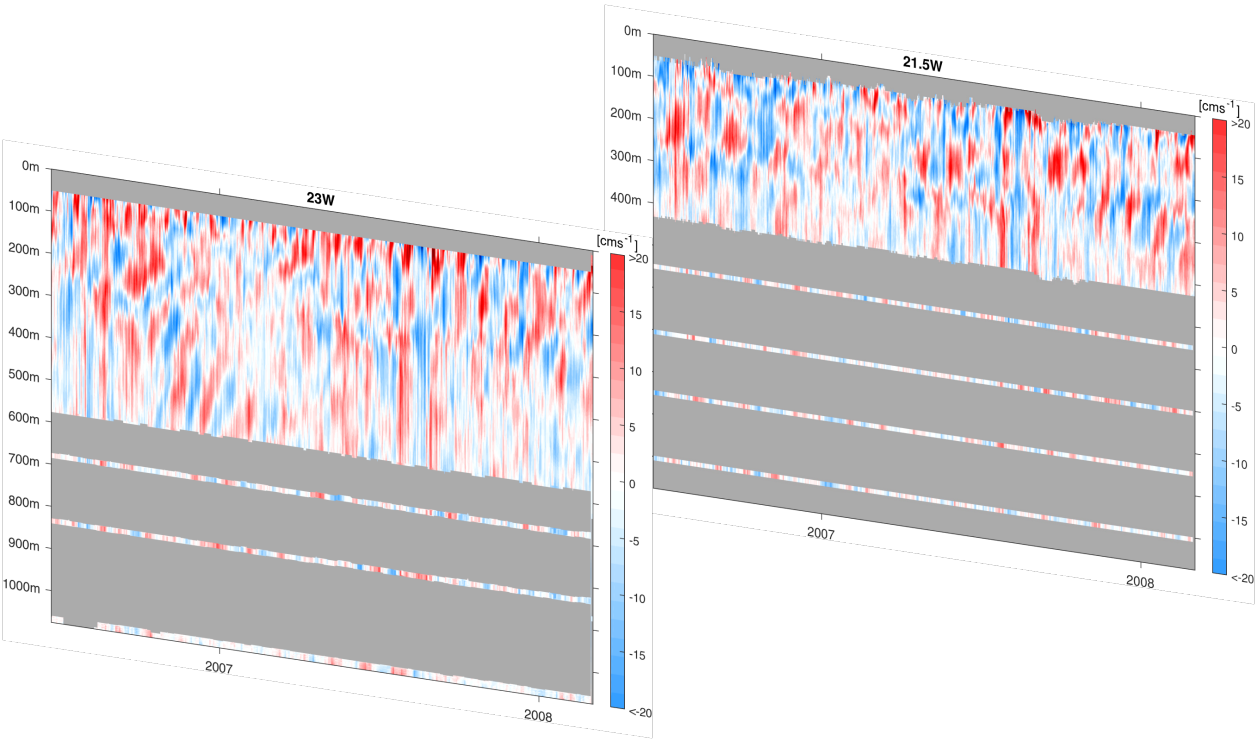

Figure 5.1: *Meridional velocity (June 2006 - March 2008) at 23° W and 21.5° W. Vertical resolution: 1m; temporal resolution: 12h. Red indicates eastward flow while blue indicates westward flow. Grey areas represent missing data. Single point measurements are expanded to 10m width around true depth.*

6 Bibliography

Ascani, F., E. Firing, P. Dutrieux, J. P. McCreary, and A. Ishida (2010), Deep equatorial ocean circulation induced by a forced- dissipated Yanai beam, *Journal of Physical Oceanography*, *40*, 1118–1142, doi:10.1175/2010JPO4356.1.

Ascani, F., E. Firing, J. P. McCreary, P. Brandt, and R. J. Greatbatch (2015), The deep equatorial ocean circulation in wind-forced numerical solutions, *Journal of Physical Oceanography*, *1*, 150429125308,004, doi:10.1175/JPO-D-14-0171.1.

Athie, G., and F. Marin (2008), Cross-equatorial structure and temporal modulation of intraseasonal variability at the surface of the Tropical Atlantic Ocean, *Journal of Geophysical Research: Oceans*, *113*, 1–17, doi:10.1029/2007JC004332.

Bourlès, B. (2003), The deep currents in the Eastern Equatorial Atlantic Ocean, *Geophysical Research Letters*, *30*(5), 8002, doi:10.1029/2002GL015095.

Brandt, P., and C. Eden (2005), Annual cycle and interannual variability of the mid-depth tropical Atlantic Ocean, *Deep Sea Research Part I: Oceanographic Research Papers*, *52*, 199–219, doi:10.1016/j.dsr.2004.03.011.

Brandt, P., F. A. Schott, C. Provost, A. Kartavtseff, V. Hormann, B. Bourlès, and J. Fischer (2006), Circulation in the central equatorial Atlantic: Mean and intraseasonal to seasonal variability, *Geophysical Research Letters*, *33*(7), 2003–2006, doi:10.1029/2005GL025498.

Brandt, P., V. Hormann, B. Bourlès, J. Fischer, F. A. Schott, L. Stramma, and M. Dengler (2008), Oxygen tongues and zonal currents in the equatorial Atlantic, *Journal of Geophysical Research: Oceans*, *113*(4), 1–15, doi:10.1029/2007JC004435.

Brandt, P., V. Hormann, A. Körtzinger, M. Visbeck, G. Krahmann, L. Stramma, R. Lumpkin, and C. Schmid (2010), Changes in the Ventilation of the Oxygen Minimum Zone of the Tropical North Atlantic, *Journal of Physical Oceanography*, *40*(i), 1784–1801, doi:10.1175/2010JPO4301.1.

Brandt, P., A. Funk, V. Hormann, M. Dengler, R. J. Greatbatch, and J. M. Toole (2011), Interannual atmospheric variability forced by the deep equatorial Atlantic Ocean., *Nature*, *473*(7348), 497–500, doi:10.1038/nature10013.

Brandt, P., A. Funk, A. Tantet, W. E. Johns, and J. Fischer (2014), The Equatorial Undercurrent in the central Atlantic and its relation to tropical Atlantic variability, *Climate Dynamics*, pp. 1–13, doi:10.1007/s00382-014-2061-4.

Brandt, P., M. Claus, R. J. Greatbatch, R. Kopte, J. M. Toole, W. E. Johns, and C. W. Böning (2016), Annual and semi-annual cycle of equatorial Atlantic circulation associated with basin mode resonance, *Journal of Physical Oceanography*, (1986), JPO–D–15–0248.1, doi:10.1175/JPO-D-15-0248.1.

Brandt, P., et al. (2012), Ventilation of the equatorial Atlantic by the equatorial deep jets, *Journal of Geophysical Research: Oceans*, *117*(12), 1–15, doi:10.1029/2012JC008118.

Bunge, L., C. Provost, and A. Kartavtseff (2007), Variability in horizontal current velocities in the central and eastern equatorial Atlantic in 2002, *Journal of Geophysical Research: Oceans*, *112*(August 2006), 1–11, doi:10.1029/2006JC003704.

Bunge, L., C. Provost, B. L. Hua, and A. Kartavtseff (2008), Variability at Intermediate Depths at the Equator in the Atlantic Ocean in 2000–06: Annual Cycle, Equatorial Deep Jets, and Intraseasonal Meridional Velocity Fluctuations, *Journal of Physical Oceanography*, *38*(8), 1794–1806, doi:10.1175/2008JPO3781.1.

Cane, M. A., and D. W. Moore (1981), A Note on Low-Frequency Equatorial Basin Modes, *Journal of Physical Oceanography*, *11*, 1578–15.

Cane, M. A., and E. Sarachik (1976), Forced baroclinic ocean motions. 1. The linear equatorial unbounded case, *Journal of Marine Research*, *34*(4), 629–665.

Chelton, D. B., F. J. Wentz, C. L. Genremann, R. a. D. Szoeke, and M. G. Schlax (2000), Satellite Microwave SST Observations of Transequatorial Tropical Instability Waves, *Geophysical Research Letters*, *27*(9), 1239–1242.

Chelton, D. B., S. K. Esbensen, M. G. Schlax, N. Thum, and M. H. Freilich (2001), Observations of coupling between surface wind stress and sea surface temperature in the eastern tropical pacific, *J. Climate*, *14*, 1479–1498.

Claus, M., R. J. Greatbatch, and P. Brandt (2014), Influence of the barotropic mean flow on the width and the structure of the Atlantic Equatorial Deep Jets, *Journal of Physical Oceanography*, *44*(9), 2485–2497, doi:10.1175/JPO-D-14-0056.1.

Claus, M., R. J. Greatbatch, P. Brandt, and J. M. Toole (2016), Forcing of the Atlantic Equatorial Deep Jets derived from Observations, *Journal of Physical Oceanography*, doi:10.1175/JPO-D-16-0140.1.

Cromwell, T., R. Montgomery, and E. Stroup (1954), Equatorial Undercurrent in Pacific Ocean Revealed by New Methods, *Science*, *119*, 648–649, doi:10.1126/science.119.3097.648.

Didwischus, S.-H. (2010), Analyse der Strukturen atlantischer äquatorialer Deep Jets anhand von Verankerungs- und Drifter-Daten, Ph.D. thesis, Kiel University.

Doherty, K. W., D. E. Frye, S. P. Liberatore, and J. M. Toole (1999), A moored profiling instrument, *Journal of Atmospheric and Oceanic Technology*, *16*(11 PART 2), 1816–1829, doi:10.1175/1520-0426(1999)016⟨1816:AMPI⟩2.0.CO;2.

D'Orgeville, M., B. L. Hua, and H. Sasaki (2007), Equatorial deep jets triggered by a large vertical scale variability within the western boundary layer, *Journal of Marine Research*, *65*, 1–25, doi:10.1357/002224007780388720.

Düing, W., et al. (1975), Meanders and long waves in the equatorial Atlantic, *Nature*, *257*, 280–284.

Eden, C., and M. Dengler (2008), Stacked jets in the deep equatorial Atlantic Ocean, *Journal of Geophysical Research: Oceans*, *113*(4), 1–12, doi:10.1029/2007JC004298.

Eriksen, C. C. (1982), Geostrophic equatorial deep jets, *Journal of Marine Research*, *40*, 143–157.

Foltz, G. R., J. A. Carton, and E. P. Chassignet (2004), Tropical instability vortices in the Atlantic Ocean, *Journal of Geophysical Research*, *109*, 1–9, doi:10.1029/2003JC001942.

Garzoli, S. L., A. Ffield, and Q. Yao (2003), North Brazil Current rings and the variability in the latitude of retroflection, *Interhemispheric Water Exchange in the Atlantic Ocean, Elsevier Oceanography Ser.*, *68*, 357–373.

Gill, A. (1982), *Atmosphere-Ocean Dynamics*, Academic Press.

Gouriou, Y., et al. (2001), Deep circulation in the equatorial Atlantic Ocean, *Geophysical Research Letters*, *28*(5), 819–822, doi:10.1029/2000GL012326.

Greatbatch, R. J., P. Brandt, M. Claus, S.-H. Didwischus, and Y. Fu (2012), On the Width of the Equatorial Deep Jets, *Journal of Physical Oceanography*, *42*(10), 1729–1740, doi:10.1175/JPO-D-11-0238.1.

Grodsky, S. A., J. A. Carton, C. Provost, J. Servain, J. A. Lorenzzetti, and M. J. McPhaden (2005), Tropical instability waves at O°N, 23°W in the Atlantic: A case study using Pilot Research Moored Array in the Tropical Atlantic (PIRATA) mooring data, *Journal of Geophysical Research C: Oceans*, *110*(8), 1–12, doi:10.1029/2005JC002941.

Hayes, S. P., and H. Milburn (1980), On the vertical structure of velocity in the eastern equatorial Pacific, doi:10.1175/1520-0485(1980)010⟨0633:OTVSOV⟩2.0.CO;2.

Hazeleger, W., P. de Vries, and Y. Friocourt (2003), Sources of the Equatorial Undercurrent in the Atlantic in a High-Resolution Ocean Model, *Journal of Physical Oceanography*, *33*(4), 677–693, doi:10.1175/1520-0485(2003)33⟨677:SOTEUI⟩2.0.CO;2.

Hua, B. L., M. D'Orgeville, M. D. Fruman, C. Menesguen, R. Schopp, P. Klein, and H. Sasaki (2008), *Destabilization of mixed Rossby gravity waves and the formation of equatorial zonal jets*, vol. 610, 311–341 pp., doi:10.1017/S0022112008002656.

Ishida, A., Y. Kashino, H. Mitsudera, N. Yoshioka, and T. Kadokura (1998), Preliminary Results of a Global High-Resolution GCM Experiment, *Journal of Faculty of Science, Hokkaido University Series VII (Geophysics)*, *11*(2), 74–93.

Jochum, M., and P. Malanotte-Rizzoli (2003), On the generation of North Brazil Current rings, *Journal of Marine Research*, *61*(2), 147–173, doi:10.1357/002224003322005050.

Jochum, M., and R. Murtugudde (2004), Internal variability of the tropical Pacific ocean, *Geophysical Research Letters*, *31*(14), 1–4, doi:10.1029/2004GL020488.

Jochum, M., P. Malanotte-Rizzoli, and A. Busalacchi (2004), Tropical instability waves in the Atlantic Ocean, *Ocean Modelling*, *7*(1-2), 145–163, doi:10.1016/S1463-5003(03)00042-8.

Jochum, M., M. F. Cronin, W. S. Kessler, and D. Shea (2007), Observed horizontal temperature advection by tropical instability waves, *Geophysical Research Letters*, *34*(9), 20–23, doi:10.1029/2007GL029416.

Johns, W. E., P. Brandt, B. Bourlès, A. Tantet, A. Papapostolou, and A. Houk (2014), Zonal structure and seasonal variability of the Atlantic Equatorial Undercurrent, *Climate Dynamics*, *43*(11), 3047–3069, doi:10.1007/s00382-014-2136-2.

Johnson, G. C. (2002), Temporal and Spatial Structure of the Equatorial Deep Jets in the Pacific Ocean, *Journal of Physical Oceanography*, *1982*(April 1982), 3396–3407, doi:10.1175/1520-0485(2002)032⟨3396:TASSOT⟩2.0.CO;2.

Johnson, G. C., and D. Zhang (2003), Structure of the Atlantic Ocean Equatorial Deep Jets, *Journal of Physical Oceanography*, *33*(3), 600–609, doi:10.1175/1520-0485(2003)033⟨0600:SOTAOE⟩2.0.CO;2.

Lumpkin, R., and S. L. Garzoli (2005), Near-surface circulation in the Tropical Atlantic Ocean, *Deep-Sea Research Part I: Oceanographic Research Papers*, *52*(3), 495–518, doi:10.1016/j.dsr.2004.09.001.

Luyten, J. R., and J. C. Swallow (1976), Equatorial undercurrents, *Deep-Sea Research and Oceanographic Abstracts*, *23*(10), 999–1001, doi:10.1016/0011-7471(76)90830-5.

Marshall, J., and R. A. Plumb (2008), *Atmosphere, Ocean, and Climate Dynamics: An Introductory Text*, Academic Press, Cleveland, doi:10.1017/CBO9781107415324.004.

McPhaden, M. J., and A. Gill (1987), Toporaphic Scattering of Equatorial Kelvin Waves, *Journal of Physical Oceanography*, *17*, 82–96.

Ménesguen, C., B. L. Hua, M. D. Fruman, and R. Schopp (2009), Dynamics of the combined extra-equatorial and equatorial deep jets in the Atlantic, *Journal of Marine Research*, *67*(3), 323–346, doi:10.1357/002224009789954766.

Metcalf, W. G., A. D. Voorhis, and M. C. Stalcup (1962), The Atlantic Equatorial Undercurrent, *Journal of Geophysical Research*, *67*(6), 2499–2508, doi:10.1029/JZ067i006p02499.

Moum, J. N., R.-C. Lien, A. Perlin, J. D. Nash, M. C. Gregg, and Wiles (2009), Sea surface cooling at the Equator by subsurface mixing in tropical instability waves, *Nature Geoscience*, *2*(11), 761–765, doi:10.1038/ngeo657.

Perez, R. C., V. Hormann, R. Lumpkin, P. Brandt, W. E. Johns, F. Hernandez, C. Schmid, and B. Bourlès (2013), Mean meridional currents in the central and eastern equatorial Atlantic, *Climate Dynamics*, pp. 1–20, doi:10.1007/s00382-013-1968-5.

Peterson, R. G., and L. Stramma (1991), Upper-level circulation in the South Atlantic Ocean, *Progress in Oceanography*, *26*(1), 1–73, doi:10.1016/0079-6611(91)90006-8.

Philander, G. (1978), Instabilities of zonal equatorial currents, 2, *Journal of Geophysical Research*, *83*, 3679–3682.

Provost, C., S. Arnault, N. Choualb, A. Kartavtseff, L. Bunge, and E. Sultan (2004), TOPEX/Poseidon and Jason Equatorial Sea Surface Slope Anomaly in the Atlantic in 2002: Comparison with Wind and Current Measurements at 23W, *Marine Geodesy*, *27*(1-2), 31–45, doi:10.1080/01490410490465274.

Qiao, L., and R. H. Weisberg (1995), Tropical instability wave kinematics: Observations from the Tropical Instability Wave Experiment, *Journal of Geophysical Research*, *100*(C5), 8677–8693, doi:10.1029/95JC00305.

Qiao, L., and R. H. Weisberg (1998), Tropical Instability Wave Energetics : Observations from the Tropical Instability Wave Experiment, *Journal of Physical Oceanography*, *28*(1988), 345–360.

Reynolds, O. (1895), On the Dynamical Theory of Incompressibl Viscous Fluids and the Determination of the Criterion, *Phil. Trans. R. Soc. London*, *186*, 123–164.

Scargle, J. D. (1982), Studies in astronomical time series analysis. II - Statistical aspects of spectral analysis of unevenly spaced data, *The Astrophysical Journal*, *263*, 835–853, doi:10.1086/160554.

Schott, F. A. (2003), The zonal currents and transports at 35°W in the tropical Atlantic, *Geophysical Research Letters*, *30*(7), 1349, doi:10.1029/2002GL016849.

Schott, F. A., J. Fischer, and L. Stramma (1998), Transports and Pathways of the Upper-Layer Circulation in the Western Tropical Atlantic, *Journal of Physical Oceanography*, *28*(10), 1904–1928, doi:10.1175/1520-0485(1998)028⟨1904:TAPOTU⟩2.0.CO;2.

Steger, J. M., and J. A. Carton (1991), Long Waves and Eddies in the Tropical Atlantic Ocean: 1984-1990, *Journal of Geophysical Research*, *96*(C8), 15,161–15,171, doi:10.1029/91JC01316.

Stramma, L., and F. A. Schott (1999), The mean flow field of the tropical Atlantic Ocean, *Deep-Sea Res. II*, *46*(1-2), 279–303, doi:10.1016/S0967-0645(98)00109-X.

von Schuckmann, K., P. Brandt, and C. Eden (2008), Generation of tropical instability waves in the Atlantic Ocean, *Journal of Geophysical Research: Oceans*, *113*(8), 1–12, doi:10.1029/2007JC004712.

Weisberg, R. H., and T. Weingartner (1988), Instability waves in the equatorial Atlantic Ocean, *Journal of Physical Oceanography*, *18*, 1641–1657.

Weisberg, R. H., A. Horigan, and C. Colin (1979), Equatorially trapped Rossby-gravity wave propagation in the Gulf of Guinea, *Journal of Marine Research*, *37*(1), 67–86.

Yu, Z., J. P. McCreary, and J. A. Proehl (1995), Meridional Asymmetry and Energetics of Tropical Instability Waves, *Journal of Physical Oceanography*, *25*, 2997–3007.

7 Erklärung

Hiermit erkläre ich, dass ich die vorliegende Arbeit selbstständig und ohne fremde Hilfe angefertigt und keine anderen als die angegebenen Quellen und Hilfsmittel verwendet habe. Die eingereichte schriftliche Fassung der Arbeit entspricht der auf dem elektronischen Speichermedium.

(Name der Datei: Tuchen-5682-Master-Thesis.pdf)

Weiterhin versichere ich, dass diese Arbeit noch nicht als Abschlussarbeit an anderer Stelle vorgelegen hat.

Ort, Datum, Unterschrift

8 Acknowledgements

I am grateful to Peter Brandt for providing this topic and for arousing my interest in the Equatorial Deep Jets since the first tropical Atlantic research cruise in spring 2014, after which I was given the chance to work further on the equatorial mooring data and to participate in two more research cruises. I am also very grateful to Martin Claus who patiently answered my countless technical and scientific questions during the last 6 months.

Thanks to my office mate Thilo for the very few constructive moments and the many non-sense talks, to Robert for the help with the harmonic fits and to my other friends for constantly supporting me during the more stressful phases of this Master Thesis.

Finally I want to thank my parents for supporting me during my Master program.